Research article

JGS
Journal of the Geological Society

Published Online First

https://doi.org/10.1144/jgs2022-090

Rift propagation in south Tibet controlled by under-thrusting of India: a case study of the Tangra Yumco graben (south Tibet)

Reinhard Wolff[1]*, Ralf Hetzel[1], Kyra Hölzer[1], István Dunkl[2], Qiang Xu[3], Aneta A. Anczkiewicz[4] and Zhenyu Li[5]

[1] Institut für Geologie und Paläontologie, Westfälische Wilhelms-Universität Münster, Corrensstraße 24, 48149 Münster, Germany
[2] Institut für Sedimentologie und Umweltgeologie, Universität Göttingen, Goldschmidtstraße 3, 37077 Göttingen, Germany
[3] CNPC Key Laboratory of Carbonate Reservoirs, Southwest Petroleum University, Xindu Avenue 8, Chengdu 610500, China
[4] Institute of Geological Sciences, Polish Academy of Sciences, Senacka 1, 31-002 Kraków, Poland
[5] State Key Laboratory of Tibetan Plateau Earth System Science, Resources and Environment, Institute of Tibetan Plateau Research, Chinese Academy of Sciences, Beijing 100101, China
RW, 0000-0002-0294-4879
* Correspondence: rwolff@uni-muenster.de

Abstract: Active graben systems in south Tibet and the Himalaya are the surface expression of ongoing east–west extension, although the cause and spatiotemporal evolution of normal faulting is a still a matter of debate. We reconstructed the exhumation history driven by normal faulting in the southern Tangra Yumco graben using new thermochronological data. The Miocene cooling history of the footwall of the main graben-bounding fault is constrained by zircon (U–Th)/He ages (16.7 ± 1.0 to 13.3 ± 0.6 Ma), apatite fission track ages (15.9 ± 2.1 to 13.0 ± 2.1 Ma) and apatite (U–Th)/He ages (7.9 ± 0.4 to 5.3 ± 0.3 Ma). Thermo-kinematic modelling of the data indicates that normal faulting began 19.0 ± 1.1 Ma at a rate of *c.* 0.2 km myr^{-1} and accelerated to *c.* 0.4 km myr^{-1} at *c.* 5 Ma. In the northern Tangra Yumco rift, remodelling of published data shows that faulting started *c.* 5 myr later at 13.9 ± 0.8 Ma. The age difference and the distance of 130 km between these two sites indicates that rifting and normal faulting propagated northward at an average rate of *c.* 25 km myr^{-1}. As this rate is similar to the Miocene convergence rate between India and south Tibet, we argue that the under-thrusting of India beneath Tibet exerted an important control on the propagation of rifts in south Tibet.

Supplementary material: Figures S1, S2, and Table S1 with details on apatite fission track analysis are available at https://doi.org/10.6084/m9.figshare.c.6198584

Received 24 June 2022; **revised** 1 September 2022; **accepted** 15 September 2022

The formation of continental rifts is associated with the growth of normal faults that accumulate displacement as they grow laterally and link with each other (e.g. Rosendahl 1987; Walsh and Watterson 1988; Cowie and Scholz 1992; Dawers *et al.* 1993; Corti 2009). Fault propagation may occur either symmetrically or asymmetrically; in the latter case, one tip of the fault remains fixed while the other fault tip advances along the strike of the fault (e.g. Schlische and Anders 1996; Morley 1999; Manighetti *et al.* 2001). As a consequence of fault growth and the initiation of new normal faults along-strike, continental rifts tend to increase in length with time. This process may proceed gradually or, alternatively, during episodes of rapid rift propagation after a new fault has been formed (e.g. Morley 1999; Corti 2009). The age of normal fault initiation along rifts is expected to be variable and becomes younger in the direction of rift propagation.

Two approaches have been applied to determine the time at which normal faults became active. The first approach is based on the analysis of sediments that were deposited in subsiding rift basins and that vary in age and thickness along rift systems (e.g. Gupta *et al.* 1998; Morley 1999; Gawthorpe and Leeder 2008). The second approach uses low-temperature thermochronology of samples from near-vertical profiles in the footwall of normal faults and takes advantage of the fact that uplifting and eroding footwalls cool over time (e.g. Armstrong *et al.* 2004; Fitzgerald *et al.* 2009). When reconstructing the history of normal faulting from thermochronological data, it is necessary to take the temporal changes in the geothermal gradient during and after faulting into account, which is best achieved using thermo-kinematic modelling (e.g. Ehlers and Farley 2003; Braun *et al.* 2012; Brown *et al.* 2017; Wolff *et al.* 2021). Changes in the geothermal gradient are caused by the advection of hot footwall rocks towards the surface during faulting and erosion, by temporal changes in the fault slip rate and by thermal relaxation after faulting has stopped (e.g. Ketcham 1996; Mancktelow and Grasemann 1997; Braun 2016; Wolff *et al.* 2020).

We determined the slip history of a range-bounding normal fault in southern Tibet by thermo-kinematic modelling of new low-temperature thermochronological data. Our results show that normal faulting in the southern Tangra Yumco graben started several million years earlier than in the northern part of the same graben, which demonstrates that normal faulting and rifting have propagated northward with time. We suggest that rift propagation was mainly controlled by under-thrusting of the Indian plate beneath Tibet, which led to crustal thickening, isostatic uplift and the initiation of normal faulting.

Tectonic evolution of the Tibetan–Himalayan orogen and rifting in south Tibet

The Tibetan–Himalayan orogen is the result of the ongoing continent–continent collision between India and Asia, which started in the Early Cenozoic (e.g. Molnar and Tapponnier 1975; Rowley 1996; Yin and Harrison 2000; Zhang *et al.* 2012). The collision was preceded by the amalgamation of the Lhasa and

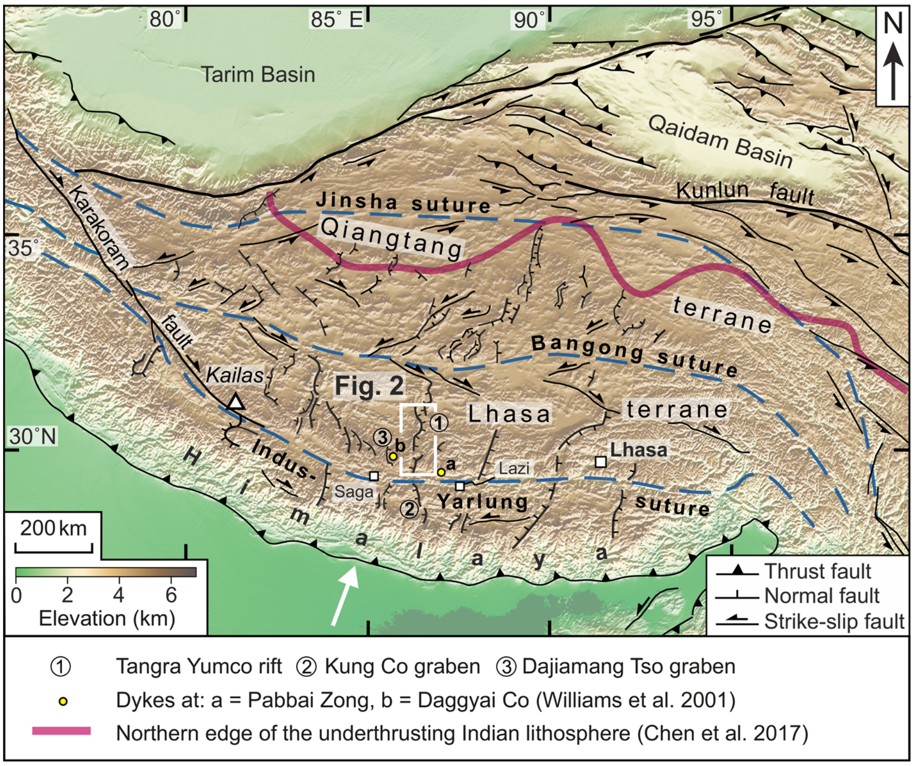

Fig. 1. Digital elevation model of the Himalaya and Tibetan Plateau showing the location of major rift systems after Tapponnier and Molnar (1977), Ratschbacher *et al.* (2011) and Wolff *et al.* (2019). The white arrow indicates the convergence vector of India relative to Asia (Ader *et al.* 2012). The white rectangle depicts the area shown in Figure 2.

Qiangtang terranes (Fig. 1) and the subduction of the Neotethyan Ocean beneath the Lhasa terrane, which caused the emplacement of voluminous S-type granitoids in the northern Lhasa terrane in the Early Cretaceous (e.g. Xu *et al.* 1985; Harris *et al.* 1990; Wen *et al.* 2008; Hetzel *et al.* 2011; Haider *et al.* 2013; Burke *et al.* 2021). During the Late Cretaceous and early Paleogene, the rollback of the Neotethyan lithosphere led to the southward migration of magmatism and the intrusion of I-type granitoids, which constitute the Gangdese Batholith (Coulon *et al.* 1986; Kapp *et al.* 2007; Wen *et al.* 2008; Zhu *et al.* 2019). The emplacement of these granitoids in the southern Lhasa terrane was accompanied by extensive volcanism that deposited the flat-lying Linzizong volcanic succession above the Gangdese Batholith (Maluski *et al.* 1982; Burg *et al.* 1983; Coulon *et al.* 1986; Lee *et al.* 2009; Liu *et al.* 2018).

After the Eocene collision of India with Asia and the formation of the Indus–Yarlung suture, a narrow sedimentary basin, the Kailas Basin, formed along the suture zone in the Oligo-Miocene (Gansser 1964; Aitchison *et al.* 2002). This basin extends from Mt Kailas in the west to the Lhasa region in the east (Fig. 1) and is dominated by conglomerates and sandstones, which were initially derived from the Gangdese arc to the north, but at later stages of basin formation also from the Xigaze forearc strata, the Indus–Yarlung suture and the Tethyan Himalaya in the south (Aitchison *et al.* 2002; DeCelles *et al.* 2011; Wang *et al.* 2013; Leary *et al.* 2016; Li *et al.* 2017). The sedimentary rocks have been referred to as the Gangrinboche Conglomerate (Aitchison *et al.* 2002), the Kailas Formation (DeCelles *et al.* 2011) or the Gangdese Conglomerate (Li *et al.* 2017); here, we use the term Kailas Formation.

Detrital zircon U–Pb dating of the basin sediments as well as $^{40}Ar/^{39}Ar$ and U–Pb ages for the intercalated tuffs and lava flows suggest that basin formation propagated from west to east (Leary *et al.* 2016). The depositional age of the Kailas Formation ranges from *c.* 26–24 Ma in the Kailas region (81° E) to *c.* 23–20 Ma at *c.* 90° E (DeCelles *et al.* 2011; Wang *et al.* 2013; Carrapa *et al.* 2014; Leary *et al.* 2016; Ai *et al.* 2022). After basin formation ceased, crustal shortening resumed and led to north-directed thrust faulting on the Great Counter Thrust system and duplex formation below the Indus–Yarlung suture (Ratschbacher *et al.* 1994; Yin *et al.* 1999; Harrison *et al.* 2000; Leary *et al.* 2016; Laskowski *et al.* 2017, 2018). The Great Counter Thrust was active in the Early Miocene, as suggested by thermochronological data and structural relationships (Sanchez *et al.* 2013; Laskowski *et al.* 2017; Orme 2019).

Several north–south-striking rift systems, some of which cut the Great Counter Thrust, have caused a significant amount of east–west extension in south Tibet (e.g. Armijo *et al.* 1986; Murphy *et al.* 2010; Ratschbacher *et al.* 2011; Styron *et al.* 2011) (Fig. 1). Rifting and extensional deformation have long been correlated with the high elevation of the plateau. Early studies hypothesized that the high elevation resulted from the removal of dense mantle lithosphere, which caused isostatic rebound and synchronous east–west extension across the Tibetan Plateau at *c.* 8 Ma (e.g. Raymo *et al.* 1988; England and Houseman 1989; Molnar *et al.* 1993). However, later studies have shown that rifting started earlier and was diachronous because most graben systems initiated between 16 and 8 Ma (e.g. Harrison *et al.* 1995; Blisniuk *et al.* 2001; Kali *et al.* 2010; McCallister *et al.* 2014; Styron *et al.* 2015; Laskowski *et al.* 2017; Wolff *et al.* 2019; Burke *et al.* 2021; Bian *et al.* 2022). Several studies have emphasized that normal faulting and extension in Tibet may be a response to crustal thickening caused by the under-thrusting of the strong Indian lower crust and mantle lithosphere beneath south Tibet (Liu and Yang 2003; Kapp and Guynn 2004; Copley *et al.* 2011; Ratschbacher *et al.* 2011; Styron *et al.* 2015). In the Lunggar rift, for example, thermo-kinematic modelling of low-temperature thermochronological data has been used to suggest that an acceleration in the rate of normal faulting occurred in the late Miocene and migrated northward ahead of the under-thrusting Indian lithosphere (Styron *et al.* 2015). If north-directed under-thrusting of India is indeed a major cause for east–west extension and rifting in south Tibet, it may also have affected the onset of normal faulting along individual graben systems. Here, we test this hypothesis for the 250 km long Tangra Yumco graben (Fig. 1), where we use new thermochronological data to determine the onset of normal faulting near the southern end of the graben.

Geology of the Tangra Yumco graben and the study area

The 250 km long Tangra Yumco rift extends from the Indus–Yarlung suture zone in the south to a dextral strike-slip fault near the Bangong suture in the north (Figs 1 and 2) (Armijo *et al.* 1986; Taylor *et al.* 2003; Wolff *et al.* 2019). There are three lakes in the graben: Tangra Yumco in the north, Xuru Co in the centre and Amu Co in the south (Fig. 2). The rivers in the northern and central graben drain into the Tangra Yumco and Xuro Co, respectively, whereas the streams in the southern graben flow south into the Dogxung-Tsangpo river, a tributary of the Yarlung-Tsangpo river. High-angle normal faults on both sides of the Tangra Yumco graben strike roughly north–south (Fig. 2). The footwall topography along the graben suggests that the main graben-bounding fault is located on the western side of the rift in the vicinity of Xuro Co and Tangra Yumco, whereas further south, in our study area, the most prominent normal fault runs along the eastern side of the graben (Fig. 3a).

The bedrock exposed in our study area consists of mainly undeformed to weakly deformed granitoid rocks of the Late Cretaceous to early Paleogene Gangdese Batholith (Fig. 3b). The intrusion age of these rocks has not been constrained in the study area. However, further north near the southern shore of the lake Tangra Yumco (Fig. 2), two granitoid samples yielded zircon U–Pb ages of 87.2 ± 0.6 and 86.6 ± 0.6 Ma (Wolff *et al.* 2019), whereas west of our study area in the Lopu Kangri region (*c.* 84.5° E), Gangdese intrusions have zircon U–Pb ages of 48.5 ± 0.5, 46.7 ± 0.7 and 38.0 ± 0.3 Ma (Laskowski *et al.* 2017). These ages are consistent with the general decrease in the age of magmatism towards the south. In our study area, the sedimentary rocks of the Kailas Formation unconformably onlap the Gangdese granitoids (Fig. 3b). South of Amu Co, the Kailas Formation has a stratigraphic thickness of *c.* 400 m and consists of conglomerates, sandstones and minor siltstones, which show flow directions toward the south to SW (Ai *et al.* 2022). The Great Counter Thrust has placed Cretaceous sedimentary rocks of the Xigaze forearc basin above the Kailas Formation (Fig. 3b) (Orme 2019; Ai *et al.* 2022). The north–south-trending normal faults of the southern Tangra Yumco graben truncate the Kailas Formation, the faults of the Great Counter Thrust and Xigaze forearc strata (Fig. 3b). Apart from the active main boundary fault at the eastern side of the graben, there is another west-dipping normal fault, which delimits a large granitoid exposure in the graben interior. South of the bedrock exposure, a *c.* 140 m high fault scarp in Quaternary sediments testifies that this normal fault is also active. The presence of the granitoid exposure in the graben interior indicates that the graben sediments are fairly thin in the study area (Fig. 3). This observation can be explained by a south-flowing stream, which removes the sedimentary material derived from the graben footwall and transports it into the Dogxung-Tsangpo river (Fig. 3a).

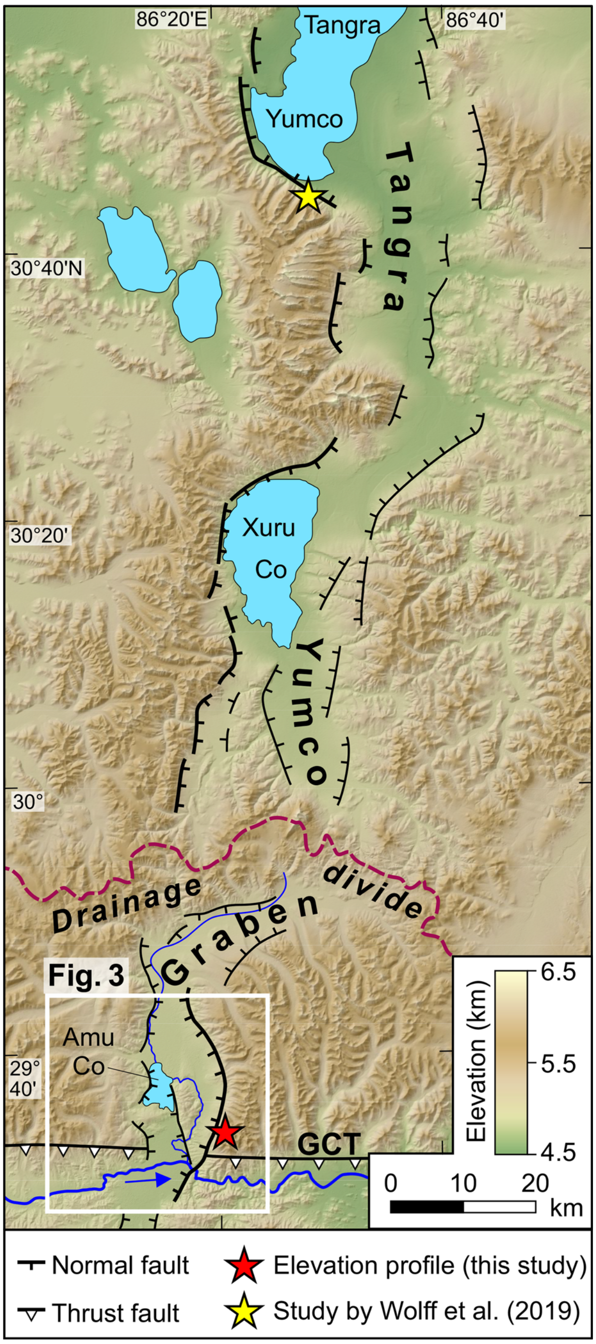

Fig. 2. Digital elevation model of the Tangra Yumco graben. Normal faults indicated with thicker lines are the major graben-bounding faults, whereas thinner lines delineate minor normal faults. The white rectangle depicts the position of our study area (Fig. 3), with the red star indicating the position of the elevation profile for thermochronology. The yellow star at the lake Tangra Yumco indicates the elevation profile of Wolff *et al.* (2019). The digital elevation model with a resolution of 1 arcsec is derived from SRTM data (Rabus *et al.* 2003). GCT, Great Counter Thrust.

Sampling for thermochronology and analytical methods

To constrain the cooling history of rocks in the southern Tangra Yumco graben, we took five undeformed granitoid samples at elevations between 4813 and 5748 m (Table 1). Four closely spaced samples were collected east of the main graben-bounding fault in the uplifted footwall along a near-vertical profile (Fig. 3), which is advantageous for determining fault slip rates with thermo-kinematic modelling (e.g. Blythe *et al.* 2007; Whipp *et al.* 2007; Wolff *et al.* 2020). The fifth sample was taken between the main boundary fault and the west-dipping normal fault in the interior of the graben (Fig. 3c). We used zircon and apatite (U–Th)/He (ZHe, AHe), as well as apatite fission track (AFT) thermochronology, on these samples. The following sections summarize the analytical procedures of the different dating techniques; a more detailed description of the analytical methods is given in Wolff *et al.* (2019).

(U–Th)/He dating

From each sample, euhedral and inclusion-free zircon and apatite crystals were selected for single-grain ZHe and AHe dating. The crystals were degassed by heating with an infrared diode laser at the GÖochron laboratories, University of Göttingen. The crystals were checked for complete degassing of He via sequential reheating and He measurements. Subsequently, the crystals were retrieved from the gas extraction line and were analysed by isotope dilution inductively coupled mass spectrometry using an APEX microflow

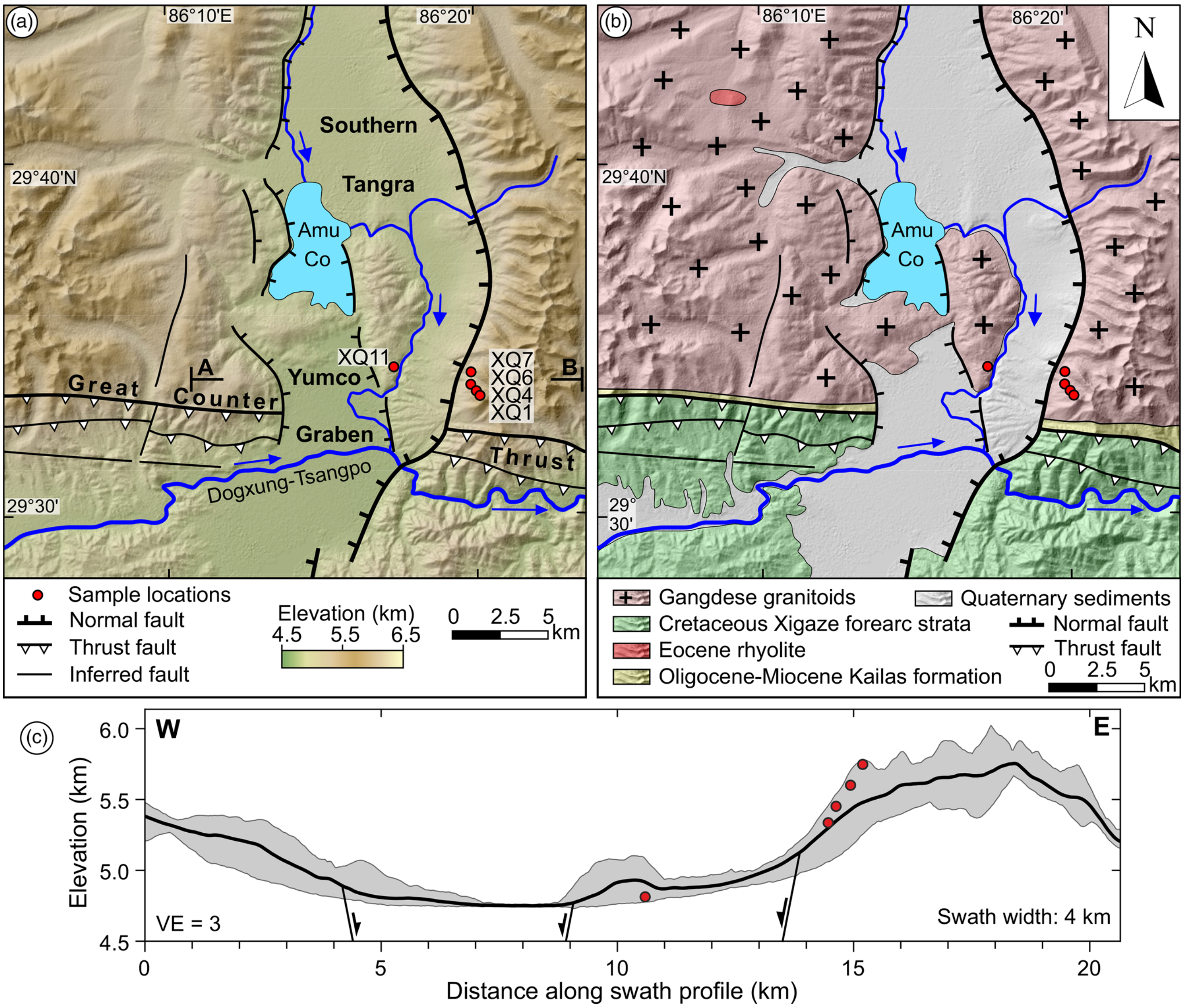

Fig. 3. (**a**) Digital elevation model of the Southern Tangra Yumco graben showing the sample locations (red dots). The younger graben-bounding normal faults cut the Great Counter Thrust fault. The line A–B depicts the position of the swath profile shown in part (c). The digital elevation model with a resolution of 1 arcsec is derived from SRTM data (Rabus *et al.* 2003). (**b**) Simplified geological map of the area shown in part (a) (modified after the 1: 250 000 geological map of the Sangsang district (Geological Survey of Jiangxi Province and Geological Survey of China 2002; Carrapa *et al.* 2014; Orme *et al.* 2015) and own observations. (**c**) Swath profile across the graben. The sampling locations (red dots) have been projected on the profile. The position of the profile is indicated in part (a).

nebulizer. Microphotographs were taken to determine the crystal shape parameters and to calculate correction factors for the ejection of α-particles (Farley *et al.* 1996) using the constants of Hourigan *et al.* (2005).

AFT dating

The AFT dating was carried out at the Institute of Geological Sciences, Polish Academy of Sciences, Kraków (Poland) using the external detector method (Gleadow 1981). Fission tracks were etched in 5 M HNO_3 at a temperature of 21°C for 20 s to reveal the spontaneous fission tracks (Zaun and Wagner 1985; Donelick *et al.* 1999). Neutron irradiation of the samples, age standards (the Fish Canyon Tuff, Durango apatite and Mount Dromedary apatite) and a CN5 glass dosimeter was performed at the TRIGA reactor at Oregon State University. The induced fission tracks in the mica detectors were revealed by etching for 45 min in 40% HF. Track counting was performed with a Nikon Eclipse E-600 microscope computer-controlled stage system with 1250× magnification. Calculations and plots were made using Trackkey software (Dunkl 2002). The fission

Table 1. *Sample locations and lithology*

Sample No.	Latitude (° N)	Longitude (° E)	Elevation (m)	Sample lithology
XQ1	29.5558	86.3354	5748	Granitoid
XQ4	29.5580	86.3335	5601	Granitoid
XQ6	29.5611	86.3305	5452	Granitoid
XQ7	29.5669	86.3307	5336	Granitoid
XQ11	29.5696	86.2934	4813	Granitoid

track ages were determined by the zeta method (Hurford and Green 1983) with the age standards listed in Hurford (1998). Error calculation followed the procedure of Green (1981).

Results

The results of the AHe and ZHe thermochronology are presented in Tables 2 and 3, respectively. The weighted mean AHe ages of the four samples in the footwall of the main rift-bounding fault are between 7.9 ± 0.4 and 5.3 ± 0.3 Ma, whereas the sample from the hanging wall yields an older age of 11.0 ± 0.5 Ma (Table 2). The mean ZHe ages of the four footwall samples range from 16.7 ± 1.0 to 13.3 ± 0.6 Ma, whereas the sample from the hanging wall again gives an older age of 21.3 ± 1.2 Ma (Table 3). The four AFT ages in the footwall range from 15.9 ± 2.1 to 13.0 ± 2.1 Ma; the hanging wall sample yields an AFT age of 12.5 ± 2.0 Ma (Table 4, Supplementary Table S1).

Our ZHe, AFT and AHe ages for the samples in the footwall of the main normal fault exhibit positive correlations between age and elevation, with the exception of the AHe age of sample XQ6 (Fig. 4). This age–elevation dependence reflects the progressive cooling of the footwall during normal faulting and exhumation. The oldest ZHe age of 16.7 ± 1.0 Ma probably provides a minimum age for the initiation of normal faulting.

The difference between the nominal values of the ZHe and the AFT ages is small (between 1.1 and 0.3 Ma), which either implies a short period of very rapid cooling (which we consider unlikely) or a lower closure temperature for the ZHe system than is commonly assumed (Guenthner *et al.* 2013; Guenthner 2021). We used thermo-kinematic modelling, as described in the next section, to decipher the history of normal faulting in more detail.

Thermo-kinematic modelling

We used the PECUBE code (version 4.2), a finite-element code that solves the three-dimensional heat transport equation and is able to predict the thermal history of fault-bounded blocks under prescribed spatially and temporally varying kinematic and topographic boundary conditions (Braun 2003; Braun *et al.* 2012). PECUBE considers temporal changes of the temperature field due to heat advection by faulting and accounts for the conduction of heat across the fault plane, which leads to a warping of the isotherms and – for normal faults – to enhanced cooling of the footwall near the fault (cf. Ehlers and Farley 2003). PECUBE also enables us to model an evolving topography, which affects the shape of the isotherms in the uppermost crust (cf. Mancktelow and Grasemann 1997) and accounts for an atmospheric lapse rate (Braun *et al.* 2012). Particle paths and the corresponding time–temperature paths are predicted for all the nodes located at the surface at the end of a model run. From these modelled temperature–time paths, PECUBE calculates cooling ages that can be directly compared with the measured cooling ages from rock samples. The misfit between the measured and modelled ages can be minimized by combining PECUBE with a two-step neighbourhood algorithm inversion, which allows an efficient exploration of the multi-dimensional parameter space by running thousands of models and yields statistically robust estimates of fault geometries, the time interval and rate of faulting, and the related exhumation. This methodology has been successfully applied to retrieve histories of faulting and landscape evolution in various geological and geomorphological settings (Braun *et al.* 2012; Glotzbach *et al.* 2013; Coutand *et al.* 2014; Styron *et al.* 2015).

All our model calculations with PECUBE were carried out on the high-performance cluster Palma-II computer at the University of Münster. Our finite-element model is 17 km long and 14 km wide to ensure that cooling ages can be predicted for all samples. The model is 70 km thick, which is similar to the present thickness of the crust in southern Tibet as derived by the receiver function method (Nábělek *et al.* 2009). The eastern boundary fault of the Tangra Yumco graben is approximated in our model by a planar fault with a dip of 60°. We begin each model run with a flat topography (i.e. zero relief) and run the model for 30 Ma. When normal faulting starts, the flat model surface evolves linearly to the present day topography, which is derived from a Shuttle Radar Topography Mission (SRTM) digital elevation model with a spatial resolution of 30 m. In all model runs, we use the following parameters and boundary conditions: a lapse rate of 6.5°C km^{-1}, a basal temperature of 800°C and a surface heat production of 5.0×10^{-6} W m^{-3}, which decreases exponentially with depth with an e-folding length of 20 km (Table 5). The thermal diffusivity κ is defined as:

$$\kappa = \frac{k}{\rho \times c_p} \tag{1}$$

where k is the thermal conductivity, c_p is the specific heat capacity and ρ is the density. Using a thermal conductivity of 2.75 J s^{-1} m^{-1} K^{-1}, a specific heat capacity of 1000 J kg^{-1} K^{-1} and a density of 2750 kg m^{-3} results in a thermal diffusivity of 1.0×10^{-6} m^2 s^{-1} (e.g. Stüwe 2007) (Table 5). These thermal parameters and boundary conditions lead to an initial geothermal gradient of 41°C km^{-1} in the upper 10 km of the model, which we consider as reasonable for thickened continental crust containing a significant fraction of granitic rocks with high concentrations of the heat-producing elements U, Th and K.

PECUBE uses time–temperature histories to calculate the apparent ages for a range of thermochronometers for samples that have reached the model surface. To compute these ages with PECUBE, we selected the He diffusion model for apatite of Farley (2000); for AFT we chose the annealing model of Ketcham (2005). The diffusion parameters of zircon depend on the density of α-damage in the crystals (Guenthner *et al.* 2013; Goldsmith *et al.* 2020; Guenthner 2021; Whipp *et al.* 2022). To account for the low radiation damage density of our zircon samples (7.7×10^{15} to 9.5×10^{16} α g^{-1}; Table 3), we adjusted the He diffusion parameters in our model towards a lower closure temperature than previously suggested by Reiners *et al.* (2004). Using a value for D_0/a^2 of 37 800 s^{-1} and an activation energy E_a of 152.5 kJ mol^{-1} results in a closure temperature of 130°C at a cooling rate of 10°C Ma^{-1} (e.g. Guenthner *et al.* 2013; Whipp *et al.* 2022). The cooling rate in our best-fit model is higher (*c.* 25°C km^{-1}), resulting in a closure temperature for zircon of *c.* 140°C. The misfit between the ages predicted by our model and the observed ages was calculated as:

$$\phi = \sum_{i=1}^{N} \left(\frac{\alpha_{i,\text{model}} - \alpha_{i,\text{data}}}{\sigma_{i,\text{data}}} \right)^2 \tag{2}$$

where N is the number of data points, $\alpha_{i,\text{data}}$ is the observed data, $\alpha_{i,\text{model}}$ is the predicted values and $\sigma_{i,\text{data}}$ is the uncertainty of the mean (U–Th)/He ages and the AFT ages.

We used an inverse modelling approach with the thermal parameters and boundary conditions defined here to minimize the misfit between the ages predicted by our PECUBE model and the ages observed in the fault footwall. The following parameters were allowed to vary within certain bounds during different model runs. The first parameter is the time when normal faulting begins in the model. We chose a time window from 22 to 16 Ma for this parameter based on the following considerations. The ZHe age of 16.7 ± 1.0 Ma for the uppermost sample in the age–elevation profile (Fig. 4) provides a minimum age for the beginning of faulting. The rift-bounding fault cross-cuts the Kailas Formation (Fig. 3b) and therefore normal faulting cannot have started before the deposition of the Kailas Formation, for which detrital U–Pb zircon dating

Table 2. *Results of apatite (U–Th)/He analysis*

Sample No.	Crystal No.	Sphere radius (µm)	Mass of crystal (µg)	He			^{238}U			^{232}Th			Th/U ratio	^{147}Sm			Ejection correction (Ft)§	Uncorrected He age (Ma)	Ft-corrected He age (Ma)	2σ (Ma)‖	Weighted mean age ± 2 s.e. (Ma)
				Vol. (ncc)*	1σ (%)	Radiation density (α g^{-1})†	Mass (ng)‡	1σ (%)	Concentration (ppm)	Mass (ng)‡	1σ (%)	Concentration (ppm)		Mass (ng)‡	1σ (%)	Concentration (ppm)					
XQ1	#1	57	2	0.081	1.2	1.29×10^{15}	0.076	1.9	31.4	0.241	2.4	99.9	3.2	0.187	2.6	77.6	0.71	5.1	7.2	0.7	
	#2	67	3	0.089	1.3	9.07×10^{14}	0.074	1.9	21.4	0.137	2.4	39.5	1.8	0.085	2.6	24.4	0.76	6.9	9.1	0.7	
	#3	57	3	0.140	1.1	2.02×10^{15}	0.147	1.8	55.7	0.291	2.4	110.7	2.0	0.229	2.6	86.9	0.71	5.4	7.6	0.7	7.9 ± 0.4
XQ4	#1	33	2	0.024	2.1	6.57×10^{14}	0.040	2.3	21.0	0.082	2.4	42.3	2.0	0.094	2.6	48.9	0.52	3.4	6.5	1.0	
	#2	51	1	0.034	1.9	1.07×10^{15}	0.035	2.4	27.6	0.138	2.4	109.7	4.0	0.198	2.6	158.0	0.67	4.1	6.2	0.7	
	#3	37	1	0.020	2.1	1.36×10^{15}	0.025	2.8	33.6	0.077	2.4	105.6	3.1	0.078	2.6	106.4	0.55	3.9	7.2	1.1	
	#4	39	1	0.034	1.6	1.48×10^{15}	0.044	2.2	41.3	0.116	2.4	108.7	2.6	0.151	2.6	141.1	0.58	3.9	6.8	0.9	6.6 ± 0.4
XQ6	#1	54	2	0.064	1.3	1.23×10^{15}	0.107	1.9	54.0	0.161	2.4	81.0	1.5	0.128	2.6	64.5	0.71	3.7	5.2	0.5	
	#2	47	2	0.049	1.7	9.02×10^{14}	0.079	1.9	35.2	0.161	2.4	71.2	2.0	0.279	2.6	123.9	0.65	3.5	5.3	0.6	
	#3	52	2	0.027	1.9	5.26×10^{14}	0.041	2.2	20.7	0.083	2.4	42.2	2.0	0.191	2.6	96.9	0.69	3.6	5.3	0.6	
	#4	49	2	0.021	2.1	5.04×10^{14}	0.027	2.7	16.1	0.078	2.4	46.8	2.9	0.102	2.6	61.1	0.67	3.8	5.7	0.7	5.3 ± 0.3
XQ7	#1	60	4	0.079	1.3	7.79×10^{14}	0.094	1.9	25.0	0.261	2.4	69.1	2.8	0.301	2.6	79.5	0.73	4.2	5.8	0.5	
	#2	52	3	0.048	1.7	6.40×10^{14}	0.066	2.0	22.5	0.192	2.4	65.4	2.9	0.202	2.6	68.9	0.69	3.6	5.2	0.5	
	#3	53	3	0.082	1.3	9.25×10^{14}	0.081	1.9	23.5	0.268	2.4	77.8	3.3	0.362	2.6	104.9	0.69	4.7	6.8	0.7	5.8 ± 0.3
XQ11	#1	60	5	0.104	1.2	7.03×10^{14}	0.084	1.9	16.2	0.206	2.4	39.5	2.4	1.113	2.6	213.3	0.73	6.1	8.5	0.8	
	#2	74	7	0.395	1.0	1.80×10^{15}	0.253	1.8	34.5	0.403	2.4	54.8	1.6	1.917	2.6	261.0	0.78	9.1	11.7	0.9	
	#3	59	6	0.503	1.0	3.00×10^{15}	0.239	1.8	39.6	1.016	2.4	168.1	4.2	3.301	2.6	546.1	0.72	8.4	11.6	1.0	
	#4	77	10	0.211	1.1	6.24×10^{14}	0.076	1.9	7.7	0.262	2.4	26.7	3.5	3.376	2.6	343.7	0.78	10.7	13.7	1.0	11.0 ± 0.5

*Amount of He is given in nano-cubic-centimetres at standard temperature and pressure.

†Radiation density is calculated according to Nasdala *et al.* (2004) using the (U–Th)/He age of the aliquot.

‡Amount of radioactive elements is given in ng.

§Ejection correction (Ft): correction factor for α-ejection according to Farley *et al.* (1996).

‖The 2σ error includes the analytical uncertainty and the estimated uncertainty of the ejection correction.

Table 3. *Results of zircon (U–Th)/He analysis*

Sample No.	Aliquot No.	Sphere radius (μm)	Mass of crystal (μg)	He			^{238}U			^{232}Th			Th/U ratio	^{147}Sm			Ejection correction (Ft)§	Uncorrected He age (Ma)	Ft-corrected He age (Ma)	2σ (Ma)‖	Weighted mean age ± 2 s.e. (Ma)
				Vol. (ncc)*	1σ (%)	Radiation density (α g^{-1})†	Mass (ng)‡	1σ (%)	Concentration (ppm)	Mass (ng)‡	1σ (%)	Concentration (ppm)		Mass (ng)‡	1σ (%)	Concentration (ppm)					
XQ1	#1	52	4	2.327	1.0	2.37×10^{16}	1.189	1.8	336.7	1.764	2.4	499.8	1.5	0.011	2.8	3.2	0.76	12.1	16.0	1.3	
	#2	*49*	*3*	*1.940*	*1.1*	*2.85×10^{16}*	*1.034*	*1.8*	*411.4*	*2.853*	*2.4*	*1135.7*	*2.8*	*0.014*	*2.8*	*5.6*	*0.74*	*9.6*	*12.9*	*1.1*	
	#3	51	4	3.104	0.9	2.78×10^{16}	1.605	1.8	402.4	1.419	2.4	355.9	0.9	0.017	2.8	4.3	0.76	13.4	17.6	1.4	16.7 ± 1.0
XQ4	#1	51	3	2.145	0.9	2.22×10^{16}	1.134	1.8	328.0	0.787	2.4	227.8	0.7	0.007	2.8	1.9	0.76	13.5	17.8	1.4	
	#2	48	3	2.651	1.0	3.27×10^{16}	1.706	1.8	580.1	0.945	2.4	321.4	0.6	0.013	2.8	4.5	0.75	11.4	15.3	1.3	16.5 ± 1.0
XQ6	#1	53	4	1.780	1.0	1.73×10^{16}	0.928	1.8	254.5	0.856	2.4	234.7	0.9	0.014	2.8	3.8	0.77	13.1	17.1	1.3	
	#2	59	4	1.219	1.0	9.53×10^{15}	0.931	1.8	212.3	0.635	2.4	144.7	0.7	0.011	2.8	2.6	0.79	9.4	11.9	0.9	
	#3	57	5	3.325	0.9	2.23×10^{16}	1.536	1.8	297.0	1.117	2.4	216.1	0.7	0.016	2.8	3.0	0.78	15.4	19.7	1.5	14.7 ± 0.7
XQ7	#1	56	3	0.995	1.0	1.05×10^{16}	0.612	1.8	184.9	0.637	2.4	192.4	1.0	0.018	2.8	5.5	0.78	10.9	14.0	1.1	
	#2	64	4	0.968	1.0	7.68×10^{15}	0.629	1.8	148.0	0.605	2.4	142.3	1.0	0.013	2.8	3.1	0.80	10.5	13.0	0.9	
	#3	54	3	0.745	1.0	9.92×10^{15}	0.508	1.9	191.9	0.494	2.4	186.6	1.0	0.010	2.8	3.9	0.77	10.0	12.9	1.0	13.3 ± 0.6
XQ11	*#1*	*47*	*2*	*2.325*	*0.9*	*4.81×10^{16}*	*0.783*	*1.8*	*444.1*	*0.340*	*2.4*	*192.8*	*0.4*	*0.008*	*2.8*	*4.6*	*0.74*	*22.4*	*30.2*	*2.6*	
	#2	52	2	3.573	5.4	5.94×10^{16}	1.934	1.8	908.5	0.552	2.4	259.4	0.3	0.009	2.8	4.0	0.76	14.4	18.8	2.5	
	#3	41	2	4.277	0.7	9.48×10^{16}	1.926	1.8	1117	0.808	2.4	468.9	0.4	0.016	1.3	9.0	0.71	16.8	23.7	2.2	
	#4	46	3	4.993	0.8	8.31×10^{16}	2.484	1.8	1125	0.920	2.4	416.5	0.4	0.011	1.3	5.0	0.74	15.4	20.9	1.8	21.3 ± 1.2

*Amount of He is given in nano-cubic-centimetres at standard temperature and pressure.
†Radiation density is calculated according to Nasdala *et al.* (2004) using the (U–Th)/He age of the aliquot.
‡Amount of radioactive elements is given in ng.
§Ejection correction (Ft): correction factor for α-ejection according to Farley *et al.* (1996).
‖The 2σ error includes the analytical uncertainty and the estimated uncertainty of the ejection correction.
¶Ages shown in italic were not considered in the calculation of the weighted mean age.

Table 4. *Results of apatite fission track analysis*

Sample No.	No. of crystals	Spontaneous		Induced		Dosimeter‡		$P(\chi^2)$§ (%)	D_{par}‖ (µm)	U (ppm)	Central age ± 1σ (Ma)¶
		ρ*	N†	ρ*	N†	ρ*	N†				
XQ1	20	0.19	65	2.99	1052	1.48	4441	99	1.99	25.8	15.9 ± 2.1
XQ4	22	0.18	45	3.00	758	1.49	4474	100	2.04	25.3	15.4 ± 2.4
XQ6	22	0.15	34	2.70	633	1.48	4430	98	2.02	22.9	13.8 ± 2.4
XQ7	23	0.14	39	2.89	781	1.49	4485	100	2.03	24.1	13.0 ± 2.1
XQ11	22	0.16	43	3.21	886	1.48	4452	100	1.87	26.8	12.5 ± 2.0

*Track densities measured as 10^6 tracks cm^{-2}.
†No. of tracks counted.
‡Dosimeter glass CN5.
§Probability of obtaining a χ^2 value for n degrees of freedom (n = no. of crystals − 1).
‖Etch pit diameter.
¶Central age was calculated according to Galbraith and Laslett (1993) with a ζ value of 348.2 ± 6.5 a cm^{-2}.

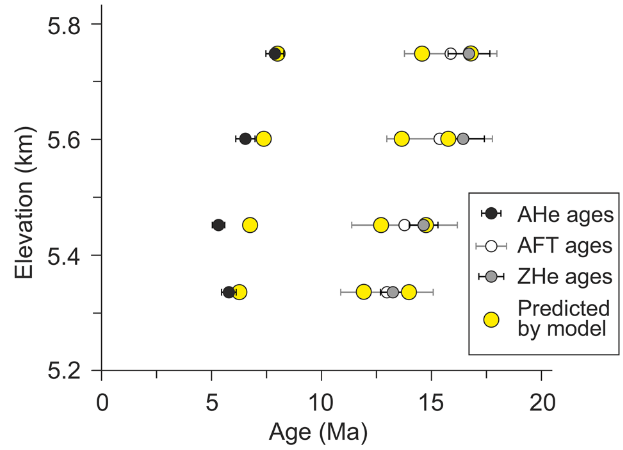

Fig. 4. Apatite (U–Th)/He (AHe), apatite fission track (AFT) and zircon (U–Th)/He (ZHe) ages and their uncertainties plotted against sample elevation (eastern footwall of the Tangra Yumco rift). Yellow points indicate ages predicted by our best-fit PECUBE model.

suggests a maximum depositional age of 21.2 ± 1.4 Ma at the nearby Geydo section (Carrapa *et al.* 2014). Because a single, temporally constant fault slip rate cannot reproduce the AHe ages and the significantly older AFT and ZHe ages at once, we subdivided the faulting history into two phases and assumed that the change in slip rate occurred between 6 and 3 Ma based on our rather young AHe ages. During the first and second phases of faulting, the slip rate was varied between 0.1 and 0.4 km myr^{-1} and from 0.2 to 0.8 km myr^{-1}, respectively. To allow an efficient exploration of the parameter space, we used a two-step neighbourhood algorithm for the inversion procedure (Sambridge 1999*a*). We performed a total of 10 000 model runs (i.e. 50 iterations with 200 model runs for each iteration) with a resampling ratio of 0.98. To derive quantitative constraints for the four free parameters and their uncertainties, we used marginal probability density functions (Sambridge 1999*b*).

The results of the inversion are shown in Figure 5, with the best-fit model indicated by a star. For the onset of normal faulting, we obtain a value of 19.0 ± 1.1 Ma, whereas the increase in fault slip occurs at 5.2 ± 0.6 Ma. The slip rates before and after the change in slip rate are 0.17 ± 0.04 and 0.41 ± 0.04 km myr^{-1}, respectively. The ZHe, AFT and AHe ages predicted by the best-fit model are shown in Figure 4, together with the observed ages. The total amount of fault slip is 4.5 ± 0.7 km, whereas the horizontal extension is 2.2 ± 0.4 km.

Remodelling of thermochronological data from the northern Tangra Yumco graben

A previous study at lake Tangra Yumco, 130 km north of our study area (yellow star in Fig. 2), also applied low-temperature thermochronology and thermo-kinematic modelling to constrain

Table 5. *Parameters of PECUBE model*

Model dimensions: length, width, thickness (km)	17, 14, 70
Temperature at base of model (°C)	800
Initial temperature at flat model surface (°C)	5
Lapse rate (°C km^{-1})	6.5
Radiogenic surface heat production (W m^{-3})	5.0 × 10^{-6}
E-folding depth (km)	20
Thermal conductivity (J s^{-1} m^{-1} K^{-1})	2.75
Specific heat capacity (J kg^{-1} K^{-1})	1000
Density (kg m^{-3})	2750
Thermal diffusivity (m^2 s^{-1})	1.0 × 10^{-6}

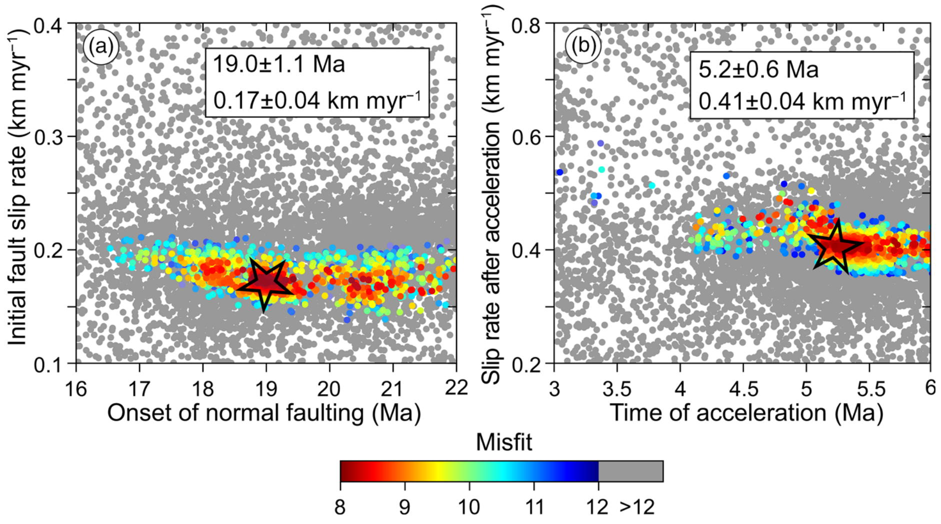

Fig. 5. Results of the inversion procedure for 10 000 PECUBE models run to determine the onset of normal faulting and the fault slip rate at the southern Tangra Yumco rift. (**a**) Projection of all model results onto a plane defined by the two free model parameters: onset of normal faulting and initial fault slip rate. Each dot corresponds to one model with the colour representing the model misfit. The star represents the best-fit model. The results suggest that normal faulting initiated at 19.0 ± 1.1 Ma with a fault slip rate of 0.17 ± 0.04 km myr^{-1}. (**b**) Projection showing the time of slip acceleration and the fault slip rate after the acceleration (star represents the best-fit model). The results indicate a slip rate of 0.41 ± 0.04 km myr^{-1} after 5.2 ± 0.6 Ma.

the history of normal faulting (Wolff *et al.* 2019). This study suggested an onset of normal faulting at 14.5 ± 1.8 Ma, but the PECUBE model differed from our current approach in three aspects. First, Wolff *et al.* (2019) used a lower thermal conductivity (2.2 J s^{-1} m^{-1} K^{-1}), which resulted in a slightly lower thermal diffusivity of 0.8 × 10^{-6} m^2 s^{-1} compared with our value of 1.0 × 10^{-6} m^2 s^{-1} (Table 5). Second, the radiogenic heat production in their model was constant, whereas we used a heat production that decreased exponentially with depth, which is more realistic. Third, Wolff *et al.* (2019) did not change the default values for He diffusion in zircon that are implemented in PECUBE, which we do here to account for the low radiation damage of the zircon samples, as explained in the previous section.

As we want to compare the timing of normal faulting in our study area with the results of Wolff *et al.* (2019) in the northern Tangra Yumco rift, we re-ran their model with the same diffusion and thermal parameters as used in this study. The results of the inverse modelling indicate that faulting in the northern Tangra Yumco rift started at 13.9 ± 0.8 Ma (Fig. S1a). Compared with the previous age constraint of 14.5 ± 1.8 Ma (Wolff *et al.* 2019), the revised age value is 0.6 Ma younger. The small difference is due to the higher thermal diffusivity of the revised model, which requires a lower amount of exhumation and therefore a later onset of normal faulting. At 2.6 ± 0.4 Ma, the slip rate in the model increases from 0.25 ± 0.03 to 0.88 ± 0.04 km myr^{-1} (Fig. S1b). The total fault slip is 5.1 ± 0.6 km, whereas the horizontal extension on the 65°-dipping fault is 2.2 ± 0.3 km. The ZHe, AFT and AHe ages measured in the northern Tangra Yumco graben and the ages predicted by the best-fit model are plotted in Figure S2.

Discussion

Onset of east–west extension and history of normal faulting

Our new AHe, AFT and ZHe ages from the southern Tangra Yumco graben reveal a progressive cooling of the footwall of the main graben-bounding normal fault since the early Miocene (Fig. 4; Tables 2–4). Our best-fit thermo-kinematic model is able to reproduce nearly all of the observed cooling ages within their uncertainties (Fig. 4). The results of the inversion procedure suggest that normal faulting initiated at 19.0 ± 1.1 Ma (Fig. 5a). This age constraint for the onset of normal faulting and rifting exceeds previous age estimates for the initiation of normal faulting in Tibet, with one exception. This exception is the Kung Co graben, located in the prolongation of the Tangra Yumco rift south of the Indus–Yarlung suture (Fig. 1), where a detailed structural study showed that ductile deformation associated with east–west extension was active during the emplacement of the Kung Co granite (Mitsuishi *et al.* 2012). Ion microprobe U–Th–Pb dating showed that the Kung Co granite intruded 18–19 myr ago (Lee *et al.* 2011), hence extensional faulting in both the southern Tangra Yumco rift and the Kung Co graben appears to have started simultaneously.

Our age estimate of 19.0 ± 1.1 Ma for the onset of normal faulting overlaps with the age of the oldest north–south-trending dykes in south Tibet, which occur east and west of the Tangra Yumco rift at Pabbai Zong and Daggyai Tso (for location, see Fig. 1). The oldest dykes at these two locations yielded Ar/Ar ages of 18.3 ± 2.7 Ma (Pabbai Zong) and 17.3 ± 1.9 Ma (Daggyai Tso), respectively, which were interpreted to date the onset of crustal extension (Williams *et al.* 2001). Although the dykes are not associated with normal faulting, they indicate an east–west orientation of the minimum principal stress σ_3 and thus a crustal stress field consistent with normal faulting on north–south-striking faults. Normal faulting started later at most of the other graben systems in south Tibet and the Himalaya, mainly between *c.* 17 and *c.* 13 Ma, although some of the extensional fault systems are even younger (e.g. Coleman and Hodges 1995; Harrison *et al.* 1995; Blisniuk *et al.* 2001; Thiede *et al.* 2006; Kali *et al.* 2010; Ratschbacher *et al.* 2011; Styron *et al.* 2013; McCallister *et al.* 2014; Laskowski *et al.* 2017; Wolff *et al.* 2019; Burke *et al.* 2021). We note that one study at the Leo Pargil gneiss dome in the western Tethyan Himalaya (*c.* 78.5° E) suggested a significantly older age of *c.* 23 Ma for the onset of extensional ductile deformation and the decompression of metamorphic rocks (Langille *et al.* 2012). This exceptionally old age may be caused by the kinematic linkage of the extensional structures at the Leo Pargil dome with the right-lateral Karakoram strike-slip fault (Langille *et al.* 2012 and references cited therein).

Our age of 19.0 ± 1.1 Ma for the beginning of normal faulting at the southern Tangra Yumco rift also provides a minimum age for the end of thrust faulting on the Great Counter Thrust in our study area because two splay faults of this thrust are cut by the high-angle normal faults of the graben (Fig. 3b). Previously reported minimum ages of 17–15 Ma for the end of faulting on the Great Counter Thrust near the towns of Saga and Lazi (for location, see Fig. 1) are slightly younger (Laskowski *et al.* 2017; Orme 2019). Our age of *c.* 19 Ma also implies that the switch from north–south contraction to east–west extension must have occurred before *c.* 16 Ma, which is the minimum age suggested by Burke *et al.* (2021) on the basis of ZHe ages in the footwall of the nearby Dajiamang Tso graben (for location, see Fig. 1).

Our best-fit PECUBE model predicts an increase in slip rate from 0.17 ± 0.04 to 0.41 ± 0.04 km myr^{-1} at 5.2 ± 0.6 Ma and a similar increase in the rate of normal faulting has been inferred at the northern Tangra Yumco graben by Wolff *et al.* (2019). The results from the re-calculated PECUBE model indicate that faulting at the northern Tangra Yumco graben accelerated *c.* 2.6 ± 0.4 Ma ago from *c.* 0.25 to *c.* 0.88 km myr^{-1} (Fig. S1). One reason for the acceleration of faulting at the two sites could be the enhanced erosion of the uplifting footwall blocks. This interpretation is based on numerical models coupling normal faulting and surface processes, which predict a more rapid fault slip if the erosion rate in the fault footwall increases (Maniatis *et al.* 2009). Faster erosion may be related to climate change in the late Miocene (e.g. Molnar 2005) and the enhancement of erosion as a result of the repeated growth of glaciers during the Quaternary ice ages (e.g. Chevalier *et al.* 2011 and references cited therein; Xu *et al.* 2021). Other, so far unknown factors, may also have contributed to the acceleration of normal faulting.

The amount of crustal extension associated with the formation of the Tangra Yumco graben is small. The slip histories derived from our PECUBE models indicate that the major normal faults in the southern and northern part of the rift caused 2.2 ± 0.4 and 2.2 ± 0.3 km of horizontal extension, respectively. The actual amount of extension should be slightly higher as a result of the presence of additional, more minor normal faults, although it is unlikely that it exceeds 3–4 km. Still, normal faulting and extension appear to be responsible for significant lateral variations in crustal conductivity because a highly conductive lower crust is present below the graben systems in south Tibet (Dong *et al.* 2020).

Exhumation of the graben interior and evolution of the Yarlung-Tsangpo river

The sediments produced by erosion of the uplifting footwall block of the southern Tangra Yumco graben are not deposited within the graben, but have largely been removed by a stream that flows south into the Dogxung-Tsangpo river (Fig. 3), a large tributary of the Yarlung-Tsangpo river. The lack of sediment deposition in the hanging wall of the graben-bounding fault is consistent with the prolonged cooling and exhumation of the bedrock exposed in the graben interior, as indicated by the cooling history of sample XQ11 (Fig. 3a). The ZHe age of 21.3 ± 1.2 Ma of this sample is older than the ZHe ages from the graben footwall and indicates cooling of the granitic bedrock before graben formation. The AFT and AHe ages for sample XQ11 of 12.5 ± 2.0 and 11.0 ± 0.5 Ma, respectively, indicate a phase of rapid cooling in the mid- to late Miocene when normal faulting and graben formation were already underway. Interestingly, a period of accelerated exhumation between *c.* 15 and *c.* 9 Ma is also evident from the cooling histories of bedrock samples taken along the braided channel of the Yarlung-Tsangpo river and its tributaries further to the east (Dai *et al.* 2021). This period of enhanced river incision may have started when the westerly flow of the Yarlung-Tsangpo river was reversed to its current eastward flow direction *c.* 15 myr ago (Wang *et al.* 2013; Li *et al.* 2017). The Dogxung-Tsangpo river and its tributary in the southern Tangra Yumco graben (Fig. 3) may have responded to this major change in the drainage network of the Yarlung-Tsangpo river with a phase of accelerated erosion and river incision. This response would explain the rapid cooling of sample XQ11 at 13–11 Ma. A subsequent phase of rapid incision of the Dogxung-Tsangpo river has formed a steep valley cutting the Xigaze forearc strata. As the spatial extent of this east–west-trending valley is restricted to the eastern footwall of the Tangra Yumco graben (Fig. 3), valley formation is the result of accelerated slip on the main graben-bounding fault since *c.* 5 Ma.

Northward propagation of normal faulting and rifting caused by the under-thrusting of India

Remodelling of the thermochronological data of Wolff *et al.* (2019) from the northern Tangra Yumco graben gives an age of 13.9 ± 0.8 Ma for the onset of normal faulting (Fig. S1), which is *c.* 5 Ma younger than the age of 19.0 ± 1.1 Ma in the southern part of the rift obtained in this study (Fig. 5a). The two different age values suggest that normal faulting in the Tangra Yumco graben started in the south and propagated towards the north, thus increasing the length of the rift over time. Based on the age difference of *c.* 5 Ma and the distance of 130 km between the two sites, the average rift propagation rate is *c.* 25 km myr^{-1} (Fig. 6). Of course, the rates at which individual normal fault segments of the Tangra Yumco graben have grown laterally may have varied through time.

NNE-directed under-thrusting of the Indian plate beneath Tibet offers a reasonable explanation for the northward propagation of rifting along the Tangra Yumco graben. Under-thrusting started after rollback and detachment of the northern part of the Indian slab, which occurred between *c.* 26 and *c.* 21 Ma and caused the formation of the Kailas Basin at low elevation and a southward shift of potassic–adakitic magmatism across the Lhasa terrane (Nomade *et al.* 2004; Chung *et al.* 2005, 2009; DeCelles *et al.* 2011; Wang *et al.* 2013; Carrapa *et al.* 2014; Leary *et al.* 2016; Chapman and Kapp 2017; Kapp and DeCelles 2019). Under-thrusting of the Indian plate beneath south Tibet predicts crustal thickening, tectonic uplift and the onset of east–west extension by normal faulting (e.g. Copeland *et al.* 1987; Zhao and Morgan 1987; Kapp and Guynn 2004; Copley *et al.* 2011; Chen *et al.* 2017; Xu *et al.* 2018). It also explains the termination of magmatism in the Lhasa terrane at 13–10 Ma (e.g. Chung *et al.* 2005; Kapp and DeCelles 2019). Under-thrusting as a mechanism for crustal extension and graben formation in Tibet requires mechanical coupling between the Tibetan upper crust and the Indian lithosphere underneath, which is indicated by the contrast in tectonic regime between dominantly normal faulting in south Tibet and primarily strike-slip faulting in central Tibet (Copley *et al.* 2011). However, the spatial difference in tectonic style should not be taken as an indicator of the position that the Indian slab has reached below Tibet (this issue is discussed in the following text) because heating of the Indian lower crust during northward movement of the slab may reduce its mechanical coupling to the Asian crust through time.

If the under-thrusting of India is responsible for the northward propagation of the Tangra Yumco rift, the average rift propagation rate of *c.* 25 km myr^{-1} estimated here should be similar to the rate of under-thrusting. Currently, the under-thrusting velocity is equivalent to the present day convergence rate between India and the Lhasa terrane if the Indian lower crust and mantle are sufficiently strong to remain undeformed while moving northward beneath Tibet (Fig. 6). Hence we interpret the geodetically determined convergence rate of 15–21 mm yr^{-1} between India and the Lhasa terrane (Ader *et al.* 2012; Zheng *et al.* 2017) as the velocity at which the Indian plate is inserted below south Tibet. Although the velocity of 15–21 mm yr^{-1} is lower than our estimate for the rate of rift propagation, the discrepancy can be explained by a 40% decrease in the total convergence rate between India and stable Asia between 20 and 10 Ma (Molnar and Stock 2009).

Using a velocity estimate of 20–25 km myr^{-1} over the last 20 Ma, we obtain a crude estimate of 400–500 km for the length of the Indian lithosphere that has been under-thrust below Tibet. This value can be compared with the amount of under-thrusting estimated from geophysical investigations (e.g. Tilmann and Ni 2003; Nábělek *et al.* 2009; Replumaz *et al.* 2014; Chen *et al.* 2017;

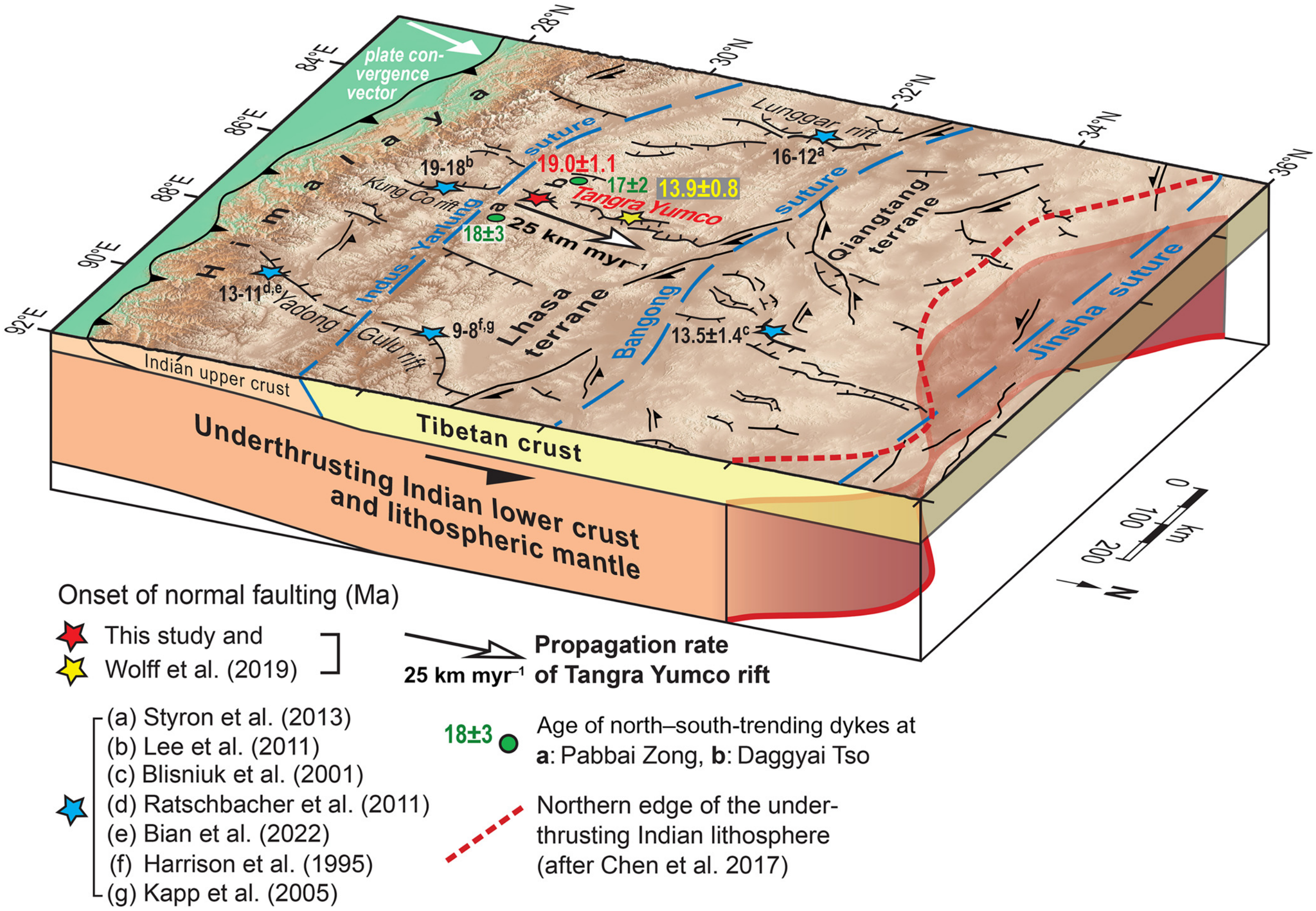

Fig. 6. Block diagram of south-central Tibet illustrating the proposed correlation between the northward propagation of the Tangra Yumco rift (black arrow with white arrowhead) and the NNE-directed under-thrusting of the lower crust and mantle lithosphere of the Indian plate beneath Tibet. Rift propagation occurred at an average rate of *c.* 25 km myr^{-1} between 19.0 ± 1.1 and 13.9 ± 0.8 Ma. The initiation ages of several well-studied rifts and the intrusion ages of north–south-trending dykes near the Tangra Yumco graben are also shown.

Li and Song 2018). These studies suggest variable amounts of under-thrusting ranging from *c.* 200 km (Nábělek *et al.* 2009) to *c.* 600 km (Chen *et al.* 2017). Although Nábělek *et al.* (2009) inferred that India's northern edge is still located below the Lhasa terrane, Chen *et al.* (2017) suggested that the northern edge of the Indian plate is irregular in shape and has already reached the Jinsha suture in some parts of the plateau (Figs 1 and 6). It is noteworthy that the northernmost Tibetan graben (located in the Qiangtang terrane at *c.* 90° E) is located above a northward bulge of the Indian plate inferred by Chen *et al.* (2017). The irregular shape of the northern edge of the Indian plate may be one reason for the spatial variations in the timing of graben formation. The spatially variable slab geometry may be related to the eastward younging of slab break-off and the formation of the Kailas Basin in the Late Oligocene–Early Miocene (Leary *et al.* 2016). Lateral differences in the thickness, temperature and composition of the Indian lithosphere and the overlying Asian crust may also have played a part (e.g. Hacker *et al.* 2000; Chan *et al.* 2009; Wolff *et al.* 2019).

Conclusions

Our new set of thermochronological data from the southern Tangra Yumco rift, together with previously published data from the northern Tangra Yumco rift, shows a younging of rift initiation from *c.* 19 Ma in the south to *c.* 14 Ma in the northern part of the rift (Fig. 6). We suggest that the northward propagation of the Tangra Yumco graben was caused by the under-thrusting of the Indian plate because our estimate for the rift propagation rate of *c.* 25 km myr^{-1} roughly fits the Miocene convergence rate between India and south Tibet. Further studies combining thermochronology and thermo-kinematic modelling in the central part of the Tangra Yumco graben and along neighbouring rifts would allow testing of this hypothesis. The spatial transition between rifting in south Tibet (i.e. the Lhasa terrane) and predominantly strike-slip faulting further north may indicate a decrease in mechanical coupling between the Indian lithosphere and the Tibetan crust, rather than the northern limit of the Indian plate below the plateau. At the Tangra Yumco rift, the three-fold acceleration in the rate of normal faulting and extension at *c.* 5 Ma (southern rift) and at *c.* 2.6 Ma (northern rift) post-dates the under-thrusting of the Indian lithosphere and must be related to other processes, such as enhanced, climate-driven erosion or a change in the tectonic boundary conditions.

Acknowledgements We thank Lin Ding for organizing the field campaign. We thank Devon A. Orme and Chen Wu for their helpful and constructive comments and the editor Renjie Zhou for editorial handling of our paper. We are grateful to Andrea Hampel for creating Figure 6 with Generic Mapping Tools (Wessel *et al.* 2013).

Author contributions **RW**: conceptualization (lead), data curation (lead), funding acquisition (equal), methodology (lead), project administration (equal), software (lead), visualization (lead), writing – original draft (lead), writing – review and editing (lead); **RH**: conceptualization (equal), funding acquisition (lead), project administration (lead), supervision (lead), writing – original draft (equal), writing – review and editing (equal); **KH**: methodology (equal), software (equal), visualization (equal), writing – original draft (equal), writing – review and editing (equal); **ID**: investigation (lead), writing – original draft (equal); **QX**: conceptualization (equal), funding acquisition (equal), investigation (equal), project administration (equal); **AAA**: investigation (equal); **ZL**: investigation (equal).

Funding This study was supported by a Joint Sino-German Research Project funded by the Natural Science Foundation of China (grant 41861134035 to Lin Ding) and the Deutsche Forschungsgemeinschaft (grants HE 1704/20-1 and WO 1949/3-1 to Ralf Hetzel and Reinhard Wolff, respectively).

Competing interests The authors declare that they have no known competing financial interests or personal relationships that could have appeared to influence the work reported in this paper.

Data availability All data generated or analysed during this study are included in this published article (and its Supplementary information files).

Scientific editing by Renjie Zhou

References

Ader, T., Avouac, J.P., Liu-Zeng, J., Lyon-Caen, H., Bollinger, L. and Galetzka, J. 2012. Convergence rate across the Nepal Himalaya and interseismic coupling on the Main Himalayan Thrust: implications for seismic hazard. *Journal of Geophysical Research: Solid Earth*, **117**, B04403, https://doi.org/10.1029/2011JB009071

Ai, K., Zhang, K., Song, B., Shen, T. and Ji, J. 2022. Upper Oligocene–Lower Miocene Gangdese Conglomerate along the Yarlung–Zangbo suture zone and its implications for Palaeo-Yarlung–Zangbo initiation. *Frontiers in Earth Science*, **10**, 808843, https://doi.org/10.3389/feart.2022.808843

Aitchison, J.C., Davis, A.M., Badengzhu and Luo, H. 2002. New constraints on the India–Asia collision: the Lower Miocene Gangrinboche conglomerates, Yarlung Tsangpo suture zone, SE Tibet. *Journal of Asian Earth Sciences*, **21**, 251–263, https://doi.org/10.1016/S1367-9120(02)00037-8

Armijo, R., Tapponnier, P., Mercier, J.L. and Han, T.L. 1986. Quaternary extension in southern Tibet: field observations and tectonic implications. *Journal of Geophysical Research: Solid Earth*, **91**, 13,803–13,872, https://doi.org/10.1029/JB091iB14p13803

Armstrong, P.A., Taylor, A.R. and Ehlers, T.A. 2004. Is the Wasatch fault footwall (Utah, United States) segmented over million-year time scales? *Geology*, **32**, 385–388, https://doi.org/10.1130/G20421.1

Bian, S., Gong, J. *et al.* 2022. Along-strike variation in the initiation timing of the north-trending rifts in southern Tibet as revealed from the Yadong–Gulu rift. *Tectonics*, **41**, e2021TC007091, https://doi.org/10.1029/2021TC007091

Blisniuk, P.M., Hacker, B.R. *et al.* 2001. Normal faulting in central Tibet since at least 13.5 Myr ago. *Nature*, **412**, 628–632, https://doi.org/10.1038/35088045

Blythe, A.E., Burbank, D.W., Carter, A., Schmidt, K. and Putkonen, J. 2007. Plio-Quaternary exhumation history of the central Nepalese Himalaya: 1. Apatite and zircon fission track and apatite (U–Th)/He analyses. *Tectonics*, **26**, TC3002, https://doi.org/10.1029/2006TC001990

Braun, J. 2003. Pecube: a new finite-element code to solve the 3D heat transport equation including the effects of a time-varying, finite amplitude surface topography. *Computers & Geosciences*, **29**, 787–794, https://doi.org/10.1016/S0098-3004(03)00052-9

Braun, J. 2016. Strong imprint of past orogenic events on the thermochronological record. *Tectonophysics*, **683**, 325–332, https://doi.org/10.1016/j.tecto.2016.05.046

Braun, J., van der Beek, P. *et al.* 2012. Quantifying rates of landscape evolution and tectonic processes by thermochronology and numerical modeling of crustal heat transport using PECUBE. *Tectonophysics*, **524–525**, 1–28, https://doi.org/10.1016/j.tecto.2011.12.035

Brown, S.J., Thigpen, J.R., Spotila, J.A., Krugh, W.C., Tranel, L.M. and Orme, D.A. 2017. Onset timing and slip history of the Teton fault, Wyoming: a multidisciplinary reevaluation. *Tectonics*, **36**, 2669–2692, https://doi.org/10.1002/2016TC004462

Burg, J.P., Proust, F., Tapponnier, P. and Ming, C.G. 1983. Deformation phases and tectonic evolution of the Lhasa block (southern Tibet, China). *Eclogae Geologicae Helvetiae*, **76**, 643–665, https://doi.org/10.5169/seals-165381

Burke, W.B., Laskowski, A.K., Orme, D.A., Sundell, K.E., Taylor, M.H., Guo, X. and Ding, L. 2021. Record of crustal thickening and synconvergent extension from the Dajiamang Tso Rift, Southern Tibet. *Geosciences*, **11**, 209, https://doi.org/10.3390/geosciences11050209

Carrapa, B., Orme, D.A., DeCelles, P.G., Kapp, P., Cosca, M.A. and Waldrip, R. 2014. Miocene burial and exhumation of the India–Asia collision zone in southern Tibet: response to slab dynamics and erosion. *Geology*, **42**, 443–446, https://doi.org/10.1130/G35350.1

Chan, G.N., Waters, D.J. *et al.* 2009. Probing the basement of southern Tibet: evidence from crustal xenoliths entrained in a Miocene ultrapotassic dyke. *Journal of the Geological Society, London*, **166**, 45–52, https://doi.org/10.1144/0016-76492007-145

Chapman, J.B. and Kapp, P. 2017. Tibetan magmatism database. *Geochemistry, Geophysics, Geosystems*, **18**, 4229–4234, https://doi.org/10.1002/2017GC007217

Chen, M., Niu, F., Tromp, J., Lenardic, A., Lee, C.-T.A., Cao, W. and Ribeiro, J. 2017. Lithospheric foundering and underthrusting imaged beneath Tibet. *Nature Communications*, **8**, 15659, https://doi.org/10.1038/ncomms15659

Chevalier, M.L., Hilley, G. *et al.* 2011. Constraints on the late Quaternary glaciations in Tibet from cosmogenic exposure ages of moraine surfaces. *Quaternary Science Reviews*, **30**, 528–554, https://doi.org/10.1016/j.quascirev.2010.11.005

Chung, S.L., Chu, M.F. *et al.* 2005. Tibetan tectonic evolution inferred from spatial and temporal variations in post-collisional magmatism. *Earth-Science Reviews*, **68**, 173–196, https://doi.org/10.1016/j.earscirev.2004.05.001

Chung, S.-L., Chu, M.-F. *et al.* 2009. The nature and timing of crustal thickening in Southern Tibet: geochemical and zircon Hf isotopic constraints from postcollisional adakites. *Tectonophysics*, **477**, 36–48, https://doi.org/10.1016/j.tecto.2009.08.008

Coleman, M. and Hodges, K. 1995. Evidence for Tibetan plateau uplift before 14 Myr ago from a new minimum age for east–west extension. *Nature*, **374**, 49–52, https://doi.org/10.1038/374049a0

Copeland, P., Harrison, T.M., Kidd, W.S., Ronghua, X. and Yuquan, Z. 1987. Rapid early Miocene acceleration of uplift in the Gangdese Belt, Xizang (southern Tibet), and its bearing on accommodation mechanisms of the India–Asia collision. *Earth and Planetary Science Letters*, **86**, 240–252, https://doi.org/10.1016/0012-821X(87)90224-X

Copley, A., Avouac, J.P. and Wernicke, B.P. 2011. Evidence for mechanical coupling and strong Indian lower crust beneath southern Tibet. *Nature*, **472**, 79–81, https://doi.org/10.1038/nature09926

Corti, G. 2009. Continental rift evolution: from rift initiation to incipient break-up in the Main Ethiopian Rift, East Africa. *Earth-Science Reviews*, **96**, 1–53, https://doi.org/10.1016/j.earscirev.2009.06.005

Coulon, C., Maluski, H., Bollinger, C. and Wang, S. 1986. Mesozoic and Cenozoic volcanic rocks from central and southern Tibet: $^{40}Ar/^{39}Ar$ dating, petrological characteristics and geodynamic implications. *Earth and Planetary Science Letters*, **79**, 281–302, https://doi.org/10.1016/0012-821X(86)90186-X

Coutand, I., Whipp, D.M., Jr, *et al.* 2014. Geometry and kinematics of the Main Himalayan Thrust and Neogene crustal exhumation in the Bhutanese Himalaya derived from inversion of multithermochronologic data. *Journal of Geophysical Research: Solid Earth*, **119**, 1446–1481, https://doi.org/10.1002/2013JB010891

Cowie, P.A. and Scholz, C.H. 1992. Growth of faults by accumulation of seismic slip. *Journal of Geophysical Research: Solid Earth*, **97**, 11,085–11,095, https://doi.org/10.1029/92JB00586

Dai, J.-G., Fox, M. *et al.* 2021. Two stages of accelerated exhumation in the middle reach of the Yarlung River, Southern Tibet since the Mid-Miocene. *Tectonics*, **40**, https://doi.org/10.1029/2020TC006618

Dawers, N.H., Anders, M.H. and Scholz, C.H. 1993. Growth of normal faults: displacement-length scaling. *Geology*, **21**, 1107–1110, https://doi.org/10.1130/0091-7613(1993)021%3C1107:GONFDL%3E2.3.CO;2

DeCelles, P.G., Kapp, P., Quade, J. and Gehrels, G.E. 2011. Oligocene–Miocene Kailas basin, southwestern Tibet: record of postcollisional upper-plate extension in the Indus–Yarlung suture zone. *GSA Bulletin*, **123**, 1337–1362, https://doi.org/10.1130/B30258.1

Donelick, R.A., Ketcham, R.A. and Carlson, W. 1999. Variability of apatite fission-track annealing kinetics; II, crystallographic orientation effects. *American Mineralogist*, **84**, 1224–1234, https://doi.org/10.2138/am-1999-0902

Dong, H., Wei, W. *et al.* 2020. Shaping the surface deformation of central and south Tibetan Plateau: insights from magnetotelluric array data. *Journal of Geophysical Research: Solid Earth*, **125**, e2019JB019206, https://doi.org/10.1029/2019JB019206

Dunkl, I. 2002. Trackkey: a Windows program for calculation and graphical presentation of fission track data. *Computers & Geosciences*, **28**, 3–12, https://doi.org/10.1016/S0098-3004(01)00024-3

Ehlers, T.A. and Farley, K.A. 2003. Apatite (U–Th)/He thermochronometry: methods and applications to problems in tectonic and surface processes. *Earth and Planetary Science Letters*, **206**, 1–14, https://doi.org/10.1016/S0012-821X(02)01069-5

England, P. and Houseman, G. 1989. Extension during continental convergence, with application to the Tibetan Plateau. *Journal of Geophysical Research*, **94**, 17,561–17,579, https://doi.org/10.1029/JB094iB12p17561

Farley, K.A. 2000. Helium diffusion from apatite: general behavior as illustrated by Durango fluorapatite. *Journal of Geophysical Research: Solid Earth*, **105**, 2903–2914, https://doi.org/10.1029/1999JB900348

Farley, K.A., Wolf, R.A. and Silver, L.T. 1996. The effects of long alpha-stopping distances on (U–Th)/He ages. *Geochimica et Cosmochimica Acta*, **60**, 4223–4229, https://doi.org/10.1016/S0016-7037(96)00193-7

Fitzgerald, P.G., Duebendorfer, E.M., Faulds, J.E. and O'Sullivan, P. 2009. South Virgin–White Hills detachment fault system of SE Nevada and NW Arizona: applying apatite fission track thermochronology to constrain the tectonic evolution of a major continental detachment fault. *Tectonics*, **28**, TC2001, https://doi.org/10.1029/2007TC002194

Galbraith, R.F. and Laslett, G.M. 1993. Statistical models for mixed fission track ages. *Nuclear tracks and radiation measurements*, **21**, 459–470, https://doi.org/10.1016/1359-0189(93)90185-C

Gansser, A. 1964. *Geology of the Himalayas*. Interscience, London.

Gawthorpe, R.L. and Leeder, M.R. 2008. Tectono-sedimentary evolution of active extensional basins. *Basin Research*, **12**, 195–218, https://doi.org/10.1111/j.1365-2117.2000.00121.x

Geological Survey of Jiangxi Province. 2002. *Geological map of the Cuomai District (Scale: 1: 250 000)*. Geological Publishing House, Beijing.

Gleadow, A.J. 1981. Fission-track dating methods: what are the real alternatives? *Nuclear Tracks and Radiation Measurements*, **5**, 3–14, https://doi.org/10.1016/0191-278X(81)90021-4

Glotzbach, C., van der Beek, P., Carcaillet, J. and Delunel, R. 2013. Deciphering the driving forces of erosion rates on millennial to million-year timescales in glacially impacted landscapes: an example from the Western Alps. *Journal of Geophysical Research: Earth Surface*, **118**, https://doi.org/10.1002/jgrf.20107

Goldsmith, A.S., Ketcham, R.A. and Stockli, D.F. 2020. Simulating effects of heterogeneous ^{4}He concentration profiles and radiation damage annealing on whole-grain zircon diffusivity analyses. *Geochimica et Cosmochimica Acta*, **284**, 239–253, https://doi.org/10.1016/j.gca.2020.05.033

Green, P.F. 1981. A new look at statistics in fission-track dating. *Nuclear Tracks and Radiation Measurements*, **5**, 77–86, https://doi.org/10.1016/0191-278X(81)90029-9

Guenthner, W.R. 2021. Implementation of an alpha damage annealing model for zircon (U–Th)/He thermochronology with comparison to a zircon fission track annealing model. *Geochemistry, Geophysics, Geosystems*, **22**, e2019GC008757, https://doi.org/10.1029/2019GC008757

Guenthner, W.R., Reiners, P.W., Ketcham, R.A., Nasdala, L. and Giester, G. 2013. Helium diffusion in natural zircon: radiation damage, anisotropy, and the interpretation of zircon (U–Th)/He thermochronology. *American Journal of Science*, **313**, 145–198, https://doi.org/10.2475/03.2013.01

Gupta, S., Cowie, P.A., Dawers, N.H. and Underhill, J.R. 1998. A mechanism to explain rift-basin subsidence and stratigraphic patterns through fault-array evolution. *Geology*, **26**, 595, https://doi.org/10.1130/0091-7613(1998)026<0595:AMTERB>2.3.CO;2

Hacker, B.R., Gnos, E. *et al.* 2000. Hot and dry deep crustal xenoliths from Tibet. *Science*, **287**, 2463–2466, https://doi.org/10.1126/science.287.5462.2463

Haider, V.L., Dunkl, I., von Eynatten, H., Ding, L., Frei, D. and Zhang, L. 2013. Cretaceous to Cenozoic evolution of the northern Lhasa Terrane and the Early Paleogene development of peneplains at Nam Co, Tibetan Plateau. *Journal of Asian Earth Sciences*, **70–71**, 79–98, https://doi.org/10.1016/j.jseaes.2013.03.005

Harris, N.B.W., Inger, S. and Xu, R.H. 1990. Cretaceous plutonism in central Tibet: an example of post-collision magmatism? *Journal of Volcanology and Geothermal Research*, **44**, 21–32, https://doi.org/10.1016/0377-0273(90)90009-5

Harrison, T.M., Copeland, P., Kidd, W.S. and Lovera, O.M. 1995. Activation of the Nyainqentanghla Shear Zone. Implications for uplift of the southern Tibetan Plateau. *Tectonics* , **14**, 658–676, https://doi.org/10.1029/95TC00608

Harrison, T.M., Yin, A., Grove, M., Lovera, O.M., Ryerson, F.J. and Zhou, X. 2000. The Zedong Window: a record of superposed Tertiary convergence in southeastern Tibet. *Journal of Geophysical Research: Solid Earth*, **105**, 19211–19230, https://doi.org/10.1029/2000JB900078

Hetzel, R., Dunkl, I., Haider, V., Strobl, M., von Eynatten, H., Ding, L. and Frei, D. 2011. Peneplain formation in southern Tibet predates the India–Asia collision and plateau uplift. *Geology*, **39**, 983–986, https://doi.org/10.1130/G32069.1

Hourigan, J., Reiners, P.W. and Brandon, M.T. 2005. U–Th zonation-dependent alpha-ejection in (U–Th)/He chronometry. *Geochimica et Cosmochimica Acta*, **69**, 3349–3365, https://doi.org/10.1016/j.gca.2005.01.024

Hurford, A. 1998. Zeta: the ultimate solution to fission-track analysis calibration or just an interim measure. *In:* van den Haute, P. and Corte, F.de (eds) *Advances in Fission-Track Geochronology*. Kluwer Academic, 19–32, https://doi.org/10.1007/978-94-015-9133-1_2

Hurford, A. and Green, P. 1983. The zeta age calibration of fission-track dating. *Chemical Geology*, **41**, 285–317, https://doi.org/10.1016/S0009-2541(83)80026-6

Kali, E., Leloup, P.H. *et al.* 2010. Exhumation history of the deepest central Himalayan rocks, Ama Drime range: key pressure–temperature–deformation–time constraints on orogenic models. *Tectonics*, **29**, 1–31, https://doi.org/10.1029/2009TC002551

Kapp, P. and DeCelles, P.G. 2019. Mesozoic–Cenozoic geological evolution of the Himalayan–Tibetan orogen and working tectonic hypotheses. *American Journal of Science*, **319**, 159–254, https://doi.org/10.2475/03.2019.01

Kapp, P. and Guynn, J.H. 2004. Indian punch rifts Tibet. *Geology*, **32**, 993–996, https://doi.org/10.1130/G20689.1

Kapp, J.L.D., Harrison, T.M., Kapp, P., Grove, M., Lovera, O.M. and Lin, D. 2005. Nyainqentanglha Shan: a window into the tectonic, thermal, and geochemical evolution of the Lhasa block, southern Tibet. *Journal of Geophysical Research: Solid Earth*, **110**, B08413, https://doi.org/10.1029/2004JB003330

Kapp, P., DeCelles, P.G. *et al.* 2007. The Gangdese retroarc thrust belt revealed. *GSA Today*, **17**, 4–9, https://doi.org/10.1130/GSAT01707A.1

Ketcham, R.A. 1996. Thermal models of core-complex evolution in Arizona and New Guinea: implications for ancient cooling paths and present-day heat flow. *Tectonics*, **15**, 933–951, https://doi.org/10.1029/96TC00033

Ketcham, R.A. 2005. Forward and inverse modeling of low-temperature thermochronometry data. *Reviews in Mineralogy & Geochemistry*, **58**, 275–314, https://doi.org/10.2138/rmg.2005.58.11

Langille, J.M., Jessup, M.J., Cottle, J.M., Lederer, G. and Ahmad, T. 2012. Timing of metamorphism, melting and exhumation of the Leo Pargil dome, northwest India. *Journal of Metamorphic Geology*, **30**, 769–791, https://doi.org/10.1111/j.1525-1314.2012.00998.x

Laskowski, A.K., Kapp, P., Ding, L., Campbell, C. and Liu, X. 2017. Tectonic evolution of the Yarlung suture zone, Lopu Range region, southern Tibet. *Tectonics*, **36**, 108–136, https://doi.org/10.1002/2016TC004334

Laskowski, A.K., Kapp, P. and Cai, F. 2018. Gangdese culmination model: Oligocene–Miocene duplexing along the India–Asia suture zone, Lazi region, southern Tibet. *GSA Bulletin*, **130**, 1355–1376, https://doi.org/10.1130/B31834.1

Leary, R., Orme, D.A., Laskowski, A.K., DeCelles, P.G., Kapp, P., Carrapa, B. and Dettinger, M. 2016. Along-strike diachroneity in deposition of the Kailas Formation in central southern Tibet: implications for Indian slab dynamics. *Geosphere*, **12**, 1198–1223, https://doi.org/10.1130/GES01325.1

Lee, H.-Y., Chung, S.L., Lo, C.H., Ji, J., Lee, T.Y., Qian, Q. and Zhang, Q. 2009. Eocene Neotethyan slab breakoff in southern Tibet inferred from the Linzizong volcanic record. *Tectonophysics*, **477**, 20–35, https://doi.org/10.1016/j.tecto.2009.02.031

Lee, J., Hager, C., Wallis, S.R., Stockli, D.F., Whitehouse, M.J., Aoya, M. and Wang, Y. 2011. Middle to late Miocene extremely rapid exhumation and thermal reequilibration in the Kung Co rift, southern Tibet. *Tectonics*, **30**, 1–26, https://doi.org/10.1029/2010TC002745

Li, J. and Song, X. 2018. Tearing of Indian mantle lithosphere from high-resolution seismic images and its implications for lithosphere coupling in southern Tibet. *Proceedings of the National Academy of Sciences of the United States of America*, **115**, 8296–8300, https://doi.org/10.1073/pnas.1717258115

Li, S., Ding, L., Xu, Q., Wang, H., Yue, Y. and Baral, U. 2017. The evolution of Yarlung Tsangpo River: constraints from the age and provenance of the Gangdese Conglomerates, southern Tibet. *Gondwana Research*, **41**, 249–266, https://doi.org/10.1016/j.gr.2015.05.010

Liu, A.L., Wang, Q. *et al.* 2018. Origin of the *c.* 50 Ma Linzizong shoshonitic volcanic rocks in the eastern Gangdese arc, southern Tibet. *Lithos*, **304–307**, 374–387, https://doi.org/10.1016/j.lithos.2018.02.017

Liu, M. and Yang, Y. 2003. Extensional collapse of the Tibetan Plateau: results of three-dimensional finite element modeling. *Journal of Geophysical Research: Solid Earth*, **108**, https://doi.org/10.1029/2002JB002248

Maluski, H., Proust, F. and Xiao, X. 1982. ^{39}Ar/^{40}Ar dating of the trans-Himalayan calc-alkaline magmatism of southern Tibet. *Nature*, **298**, 152–154, https://doi.org/10.1038/298152a0

Mancktelow, N.S. and Grasemann, B. 1997. Time-dependent effects of heat advection and topography on cooling histories during erosion. *Tectonophysics*, **270**, 167–195, https://doi.org/10.1016/S0040-1951(96)00279-X

Maniatis, G., Kurfeß, D., Hampel, A. and Heidbach, O. 2009. Slip acceleration on normal faults due to erosion and sedimentation – results from a new three-dimensional numerical model coupling tectonics and landscape evolution. *Earth and Planetary Science Letters*, **284**, 570–582, https://doi.org/10.1016/j.epsl.2009.05.024

Manighetti, I., King, G.C.P., Gaudemer, Y., Scholz, C.H. and Doubre, C. 2001. Slip accumulation and lateral propagation of active normal faults in Afar. *Journal of Geophysical Research: Solid Earth*, **106**, 13,667–13,696, https://doi.org/10.1029/2000JB900471

McCallister, A.T., Taylor, M.H., Murphy, M.A., Styron, R.H. and Stockli, D.F. 2014. Thermochronologic constraints on the late Cenozoic exhumation history of the Gurla Mandhata metamorphic core complex, southwestern Tibet. *Tectonics*, **33**, 27–52, https://doi.org/10.1002/2013TC003302

Mitsuishi, M., Wallis, S.R., Aoya, M., Lee, J. and Wang, Y. 2012. E–W extension at 19 Ma in the Kung Co area, S. Tibet: evidence for contemporaneous E–W and N–S extension in the Himalayan orogen. *Earth and Planetary Science Letters*, **325–326**, 10–20, https://doi.org/10.1016/j.epsl.2011.11.013

Molnar, P. 2005. Mio-Pliocene growth of the Tibetan Plateau and evolution of East Asian climate. *Palaeontologia Electronica*, **8**, 1–23.

Molnar, P. and Stock, J.M. 2009. Slowing of India's convergence with Eurasia since 20 Ma and its implications for Tibetan mantle dynamics. *Tectonics*, **28**, TC3001, https://doi.org/10.1029/2008TC002271

Molnar, P. and Tapponnier, P. 1975. Cenozoic tectonics of Asia: effects of a continental collision. *Science*, **189**, 419–426, https://doi.org/10.1126/science.189.4201.419

Molnar, P., England, P. and Martinod, J. 1993. Mantle dynamics, uplift of the Tibetan Plateau, and the Indian monsoon. *Reviews of Geophysics*, **31**, 357–396, https://doi.org/10.1029/93RG02030

Morley, C.K. 1999. Patterns of displacement along large normal faults: implications for basin evolution and fault propagation, based on examples from East Africa. *AAPG Bulletin*, **83**, 613–634, https://doi.org/10.1306/00AA9C0A-1730-11D7-8645000102C1865D

Murphy, M.A., Sanchez, V. and Taylor, M.H. 2010. Syncollisional extension along the India–Asia suture zone, south-central Tibet: implications for crustal deformation of Tibet. *Earth and Planetary Science Letters*, **290**, 233–243, https://doi.org/10.1016/j.epsl.2009.11.046

Nábělek, J., Hetényi, G. *et al.* 2009. Underplating in the Himalaya–Tibet collision zone revealed by the Hi-CLIMB experiment. *Science*, **325**, 1371–1374, https://doi.org/10.1126/science.1167719

Nasdala, L., Reiners, P.W., Garver, J.I., Kennedy, A.K., Stern, R.A., Balan, E. and Wirth, R. 2004. Incomplete retention of radiation damage in zircon from

Sri Lanka. *American Mineralogist*, **89**, 219–231, https://doi.org/10.2138/am-2004-0126

Nomade, S., Renne, P.R., Mo, X., Zhao, Z. and Zhou, S. 2004. Miocene volcanism in the Lhasa block, Tibet: spatial trends and geodynamic implications. *Earth and Planetary Science Letters*, **221**, 227–243, https://doi.org/10.1016/S0012-821X(04)00072-X

Orme, D.A. 2019. Burial and exhumation history of the Xigaze forearc basin, Yarlung suture zone, Tibet. *Geoscience Frontiers*, **10**, 895–908, https://doi.org/10.1016/j.gsf.2017.11.011

Orme, D.A., Carrapa, B. and Kapp, P. 2015. Sedimentology, provenance and geochronology of the upper Cretaceous–lower Eocene western Xigaze forearc basin, southern Tibet. *Basin Research*, **27**, 387–411, https://doi.org/10.1111/bre.12080

Rabus, B., Eineder, M., Roth, A. and Bamler, R. 2003. The Shuttle Radar Topography Mission – a new class of digital elevation models acquired by spaceborne radar. *ISPRS Journal of Photogrammetry and Remote Sensing*, **57**, 241–262, https://doi.org/10.1016/S0924-2716(02)00124-7

Ratschbacher, L., Frisch, W., Liu, G. and Chen, C. 1994. Distributed deformation in southern and western Tibet during and after the India–Asia collision. *Journal of Geophysical Research: Solid Earth*, **99**, 19,917–19,945, https://doi.org/10.1029/94JB00932

Ratschbacher, L., Krumrei, I. *et al.* 2011. Rifting and strike-slip shear in central Tibet and the geometry, age and kinematics of upper crustal extension in Tibet. *Geological Society, London, Special Publications*, **353**, 127–163, https://doi.org/10.1144/SP353.8

Raymo, M.E., Ruddiman, W.F. and Froelich, P.N. 1988. Influence of late Cenozoic mountain building on ocean geochemical cycles. *Geology*, **16**, 649–653, https://doi.org/10.1130/0091-7613(1988)016<0649:IOLCMB>2.3.CO;2

Reiners, P.W., Spell, T.L., Nicolescu, S. and Zanetti, K.A. 2004. Zircon (U–Th)/He thermochronometry: He diffusion and comparisons with $^{40}Ar/^{39}Ar$ dating. *Geochimica et Cosmochimica Acta*, **68**, 1857–1887, https://doi.org/10.1016/j.gca.2003.10.021

Replumaz, A., Capitanio, F.A., Guillot, S., Negredo, A.M. and Villaseñor, A. 2014. The coupling of Indian subduction and Asian continental tectonics. *Gondwana Research*, **26**, 608–626, https://doi.org/10.1016/j.gr.2014.04.003

Rosendahl, B.L. 1987. Architecture of continental rifts with special reference to east Africa. *Annual Reviews of Earth and Planetary Sciences*, **15**, 445–503, https://doi.org/10.1146/annurev.ea.15.050187.002305

Rowley, D.B. 1996. Age of initiation of collision between India and Asia: a review of stratigraphic data. *Earth and Planetary Science Letters*, **145**, 1–13, https://doi.org/10.1016/S0012-821X(96)00201-4

Sambridge, M. 1999*a*. Geophysical inversion with a neighbourhood algorithm – I. Searching a parameter space. *Geophysical Journal International*, **138**, 479–494, https://doi.org/10.1046/j.1365-246X.1999.00876.x

Sambridge, M. 1999*b*. Geophysical inversion with a neighbourhood algorithm – II. Appraising the ensemble. *Geophysical Journal International*, **138**, 727–746, https://doi.org/10.1046/j.1365-246x.1999.00900.x

Sanchez, V.I., Murphy, M.A., Robinson, A.C., Lapen, T.J. and Heizler, M.T. 2013. Tectonic evolution of the India–Asia suture zone since Middle Eocene time, Lopukangri area, south-central Tibet. *Journal of Asian Earth Sciences*, **62**, 205–220, https://doi.org/10.1016/j.jseaes.2012.09.004

Schlische, R.W. and Anders, M.N. 1996. Stratigraphic effects and tectonic implications of the growth of normal faults and extensional basins. *GSA, Special Papers*, **303**, 183–203, https://doi.org/10.1130/0-8137-2303-5.183

Stüwe, K. 2007. *Geodynamics of the Lithosphere*. 2nd edn. Springer, Berlin.

Styron, R.H., Taylor, M.H. and Murphy, M.A. 2011. Oblique convergence, arc-parallel extension, and the role of strike-slip faulting in the High Himalaya. *Geosphere*, **7**, 582–596, https://doi.org/10.1130/GES00606.1

Styron, R.H., Taylor, M.H. *et al.* 2013. Miocene initiation and acceleration of extension in the South Lunggar rift, western Tibet: evolution of an active detachment system from structural mapping and (U–Th)/He thermochronology. *Tectonics*, **32**, 1–28, https://doi.org/10.1002/tect.20053

Styron, R., Taylor, M. and Sundell, K. 2015. Accelerated extension of Tibet linked to the northward underthrusting of Indian crust. *Nature Geoscience*, **8**, 131–134, https://doi.org/10.1038/ngeo2336

Tapponnier, P. and Molnar, P. 1977. Active faulting and tectonics in China. *Journal of Geophysical Research*, **82**, 2905–2930, https://doi.org/10.1029/JB082i020p02905

Taylor, M., Yin, A., Ryerson, F.J., Kapp, P. and Ding, L. 2003. Conjugate strike-slip faulting along the Bangong–Nujiang suture zone accommodates coeval east–west extension and north–south shortening in the interior of the Tibetan Plateau. *Tectonics*, **22**, 1–25, https://doi.org/10.1029/2002TC001361

Thiede, R.C., Arrowsmith, J.R., Bookhagen, B., McWilliams, M., Sobel, E.R. and Strecker, M.R. 2006. Dome formation and extension in the Tethyan Himalaya, Leo Pargil, northwest India. *GSA Bulletin*, **118**, 635–650, https://doi.org/10.1130/B25872.1

Tilmann, F. and Ni, J. and INDEPTH III seismic team 2003. Seismic imaging of the downwelling Indian lithosphere beneath central Tibet. *Science*, **300**, 1424–1427, https://doi.org/10.1126/science.1082777

Walsh, J.J. and Watterson, J. 1988. Analysis of the relationship between displacements and dimensions of faults. *Journal of Structural Geology*, **10**, 239–247, https://doi.org/10.1016/0191-8141(88)90057-0

Wang, J.-G., Hu, X.-M., Garzanti, E. and Wu, F.-Y. 2013. Upper Oligocene–Lower Miocene Gangrinboche conglomerate in the Xigaze area, southern Tibet: implications for Himalayan uplift and Paleo-Yarlung–Zangbo initiation. *The Journal of Geology*, **121**, 425–444, https://doi.org/10.1086/670722

Wen, D.R., Liu, D.Y. *et al.* 2008. Zircon SHRIMP U–Pb ages of the Gangdese Batholith and implications for Neotethyan subduction in southern Tibet. *Chemical Geology*, **252**, 191–201, https://doi.org/10.1016/j.chemgeo.2008.03.003

Wessel, P., Smith, W.H.F., Scharroo, R., Luis, J. and Wobbe, F. 2013. Generic mapping tools: improved version released. *Eos*, **94**, 409–410, https://doi.org/10.1002/2013EO450001

Whipp, D.M., Ehlers, T.A., Blythe, A.E., Huntington, K.W., Hodges, K.V. and Burbank, D.W. 2007. Plio-Quaternary exhumation history of the central Nepalese Himalaya: 2. Thermokinematic and thermochronometer age prediction model. *Tectonics*, **26**, TC3003, https://doi.org/10.1029/2006TC001991

Whipp, D.M., Kellett, D.A., Coutand, I. and Ketcham, R.A. 2022. Short communication: modeling competing effects of cooling rate, grain size, and radiation damage in low-temperature thermochronometers. *Geochronology*, **4**, 143–152, https://doi.org/10.5194/gchron-4-143-2022

Williams, H., Turner, S., Kelley, S. and Harris, N. 2001. Age and composition of dikes in southern Tibet: new constraints on the timing of east–west extension and its relationship to postcollisional volcanism. *Geology*, **29**, 339–342, https://doi.org/10.1130/0091-7613(2001)029<0339:AACODI>2.0.CO;2

Wolff, R., Hetzel, R., Dunkl, I., Xu, Q., Bröcker, M. and Anczkiewicz, A.A. 2019. High-angle normal faulting at the Tangra Yumco graben (southern Tibet) since *c.* 15 Ma. *The Journal of Geology*, **127**, 15–36, https://doi.org/10.1086/700406

Wolff, R., Hetzel, R., Dunkl, I., Anczkiewicz, A.A. and Pomella, H. 2020. Fast cooling of normal-fault footwalls: rapid fault slip or thermal relaxation? *Geology*, **48**, 333–337, https://doi.org/10.1130/G46940.1

Wolff, R., Hetzel, R., Dunkl, I. and Anczkiewicz, A.A. 2021. New constraints on the exhumation history of the western Tauern Window (European Alps) from thermochronology, thermokinematic modeling, and topographic analysis. *International Journal of Earth Sciences*, **110**, 2955–2977, https://doi.org/10.1007/s00531-021-02094-w

Xu, R.H., Schärer, U. and Allègre, C.J. 1985. Magmatism and metamorphism in the Lhasa block (Tibet): a geochronological study. *The Journal of Geology*, **93**, 41–57, https://doi.org/10.1086/628918

Xu, Q., Ding, L., Spicer, R.A., Liu, X., Li, S. and Wang, H. 2018. Stable isotopes reveal southward growth of the Himalayan–Tibetan Plateau since the Paleocene. *Gondwana Research*, **54**, 50–61, https://doi.org/10.1016/j.gr.2017.10.005

Xu, Z., Wan, S. *et al.* 2021. Enhancements of Himalayan and Tibetan erosion and the produced organic carbon burial in distal tropical marginal seas during the Quaternary glacial periods: an integration of sedimentary records. *Journal of Geophysical Research: Earth Surface*, **126**, e2020JF005828, https://doi.org/10.1029/2020JF005828

Yin, A. and Harrison, T.M. 2000. Geologic evolution of the Himalayan–Tibetan Orogen. *Annual Review of Earth and Planetary Sciences*, **28**, 211–280, https://doi.org/10.1146/annurev.earth.28.1.211

Yin, A., Harrison, T.M. *et al.* 1999. Tertiary deformation history of southeastern and southwestern Tibet during the Indo-Asian collision. *GSA Bulletin*, **111**, 1644–1664, https://doi.org/10.1130/0016-7606(1999)111<1644:TDHOSA>2.3.CO;2

Zaun, P. and Wagner, G.A. 1985. Fission track stability in zircon under geological conditions. *Nuclear Tracks and Radiation Measurements*, **10**, 303–307, https://doi.org/10.1016/0735-245X(85)90119-X

Zhang, Q., Willems, H., Ding, L., Gräfe, K.-U. and Appel, E. 2012. Initial India–Asia continental collision and foreland basin evolution in the Tethyan Himalaya of Tibet: evidence from stratigraphy and paleontology. *The Journal of Geology*, **120**, 175–189, https://doi.org/10.1086/663876

Zhao, W.-L. and Morgan, W.J. 1987. Injection of Indian crust into Tibetan lower crust: a two-dimensional finite element model study. *Tectonics*, **6**, 489–504, https://doi.org/10.1029/TC006i004p00489

Zheng, G., Wang, H. *et al.* 2017. Crustal deformation in the India–Eurasia collision zone from 25 years of GPS measurements. *Journal of Geophysical Research: Solid Earth*, **122**, 9290–9312, https://doi.org/10.1002/2017JB014465

Zhu, D.C., Wang, Q., Chung, S.L., Carood, P.A. and Zhao, Z.D. 2019. Gangdese magmatism in southern Tibet and India–Asia convergence since 120 Ma. *Geological Society, London, Special Publications*, **483**, 583–604, https://doi.org/10.1144/SP483.14